Tribology International 210 (2025) 110776

Contents lists available at ScienceDirect

Tribology International

journal homepage: www.elsevier.com/locate/triboint

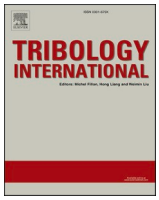

Effect of current discharges across MTM and MPR tribological contacts with negatively charged MTM ball and MPR roller

G. Cernalevschi [a], M. Ratoi [a,*], B.G. Mellor [a], Y. Cai [b]

[a] Faculty of Engineering and Physical Sciences, University of Southampton, Southampton, United Kingdom
[b] ESSO Deutschland GmbH, Hamburg, Germany

ARTICLE INFO

Keywords:
Electrical discharges
Cathodic polarity
Current density
RCF

ABSTRACT

Stray currents in wind turbines have been associated with the premature failure of bearings through lubricant degradation and wear mechanisms. Tribological contacts under electrical current flow can be described as electrolytic cells, where the interacting bodies act as cathode and anode. This study investigated how cathodic polarity and current densities in tribological contacts impact tribofilm formation and wear mechanisms. Applied voltages higher than the dielectric strength of the oil enabled current flow across the tribological contact. The tribofilm predominately formed on the anode which attracted dissociated anions from additives and increased with current density, while the cathode remained unprotected. The damage on the cathode took the form of micro-pitting, wavelets and at low current densities, sub-surface WECs surrounded by WEAs.

1. Introduction

Based on "Statistical Review of World Energy", in 2023, the cumulative global installation capacity of wind power was 1017.2 GW; this had increased by 12.9 % over 2022–2023 [1]. In spite of this, the failure rate of the modern utility-scale wind turbines continues to be high (failure/turbine/year >1) [2] because of the harsh conditions of operation. The greatest downtime is due to generator and gearbox problems [3], with the bearings being the most affected parts e.g. a failure rate of 90 % [4]. The failure modes have been attributed to wear, cracks and fracture, plastic deformation, lubricant failures, contact fatigue, manufacturing and operating problems, and electrical erosion [5].

Apart from the challenges posed by the mechanical and environmental conditions of operation, wind turbine bearings are affected by stray currents, an undesirable and harmful phenomenon that has three main causes: (I) electrostatic charging of the wind turbine blades, which results in a DC current circulating through the drivetrain and discharges taking place at the main shaft, gearbox, or generator bearings (in gearless turbines) [6–12]; (II) magnetic flux asymmetries leading to a shaft voltage being induced in the axial direction and low-frequency AC currents flowing through generator bearings [13–15]; and (III) common-mode voltage in combination with high slew rates of the voltage pulses lead to high-frequency AC currents affecting the generator or gearbox bearings [16–19]. These currents lead to earlier failure of wind turbine bearings through wear mechanisms such as: frosting [20–22], fluting [21,23,24], pitting [25,26], insulation coatings breakdown [27,28], white etching cracks (WECs) [29–39], lubricant degradation [40,41].

The effect of small DC electrical currents (< 25 μA) from electrostatic charges [36] and high DC/AC electrical currents (densities > 0.01 A/mm^2) [34] on WEC formation in roller bearings lubricated with an automotive gearbox oil SAE 75W-80 [36] and a synthetic industrial gearbox oil ISO VG 320 [34] was investigated. Two hypotheses for WEC formation were proposed by the authors: (I) 'Cathodic WEC fatigue' affecting predominantly the negatively charged cathodic rings which is triggered by small DC currents and lubricant formulation which produces hydrogen cations (H^+) that diffuse beneath the surface to promote WEC formation and propagation [36]; and (II) 'Energetic WEC fatigue' affecting mainly the positive anodic rings produced by high DC/AC currents that exceed the dielectric strength of the lubricant and lead to electrical discharges and increased local temperatures. This generates hydrogen radicals (H•) from lubricant/water molecules and leads to failure at the anode from WEC [34]. A study on the effect of DC currents on WEC formation on a three-ring-on-roller ZF-type tribometer lubricated with a commercial mineral oil ISO VG 100 found that both polarities (cathodic or anodic) in combination with specific test conditions

* Correspondence to: Department of Mechanical Engineering, Faculty of Engineering and Physical Sciences, University of Southampton, Highfield Campus, Southampton, SO17 1BJ, United Kingdom.
E-mail address: m.ratoi@soton.ac.uk (M. Ratoi).

https://doi.org/10.1016/j.triboint.2025.110776
Received 20 December 2024; Received in revised form 18 March 2025; Accepted 5 May 2025
Available online 8 May 2025

Table 1
MTM-SLIM electrical setup test conditions.

Test conditions	Conditioning phase	Stribeck phase
Applied voltage interval (V)[I]	0 – 5	
Applied voltage (V)[II]	1.4/ 1.6	
Balance resistance (Ω)[I, II]	10/ 100	
Load (N)	50	
Max stress (GPa)	1.1	
SRR (%)	- 30	
Temperature (° C)	100	
Entrainment speed (m/s)[I]	0.2	
Entrainment speed (m/s)	0.1	2–0.01
Time interval (min)	-	0, 1, 5, 10, 20, 60, 120, 180

[I] I-V curves; [II] Testing routine

Table 2
Test conditions for MPR fatigue tests.

	Oil type
Test conditions	Gearbox oil
Duration (h)	288
Contact type	Line
Load (N)	500
Max stress (GPa)	1.92
SRR (%)	- 30
Rolling speed (m/s)	3.4
Temperature (°C)	100
Applied voltage interval (V)[I]	0 – 5
Applied voltage (V)[II]	- 1, - 3
Balance resistance (Ω)[I, II]	5
Film thickness (nm)	98.6
Lambda	0.69
CLA acceleration (g)	5
Peak to peak acceleration (g)	15

[I] I-V curves; [II] Testing routine

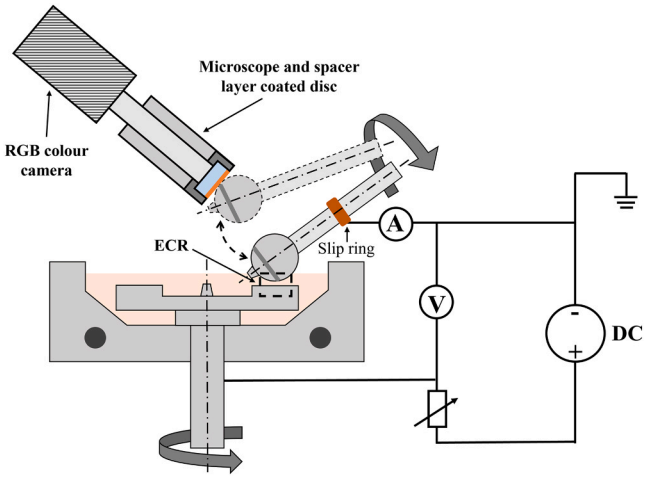

Fig. 1. Schematic representation of the electrical circuit setup connected to MTM.

such as load, SRR and contact current density can lead to earlier WECs in anodic specimens [33]. Current densities $> 0.75\,A/mm^2$ were also shown to lead to failures from electrical erosion and the tribofilm composition depended on the polarity of specimens. The authors assumed that WEC failures under electrical conditions can be attributed to the roughening of surfaces from electrical discharges producing alternating stresses in the sub-surface or hydrogen release from the lubricant. The lubricant used in these studies initiated WEC formation even in absence of electrical current [42–44], which made it difficult to separate the effect of the current from that of the lubricant.

The functionality of 'Cathodic/Energetic WEC fatigue' hypotheses has been refuted by a study which used perfluoropolyether (PFPE) base oil to lubricate RCF tests [35]. The authors investigated the effect of DC currents on WEC formation in the Micro-Pitting Rig under large currents (250 mA) and found no correlation with atomic hydrogen. When commercially fully formulated WT gearbox lubricants were used, WEC failure took place at applied current values of > 25 mA and WEC started from the local plastic deformation, due to combined cyclic stresses and electrically aided dislocation motion around stress concentrators, the time-to-failure depending on the lubricant base oil type and the additive package. The investigation using AC current [32] found that the time-to-failure decreases with increase of the AC current magnitude, with macro-pitting as the dominant failure mechanism. In addition, WECs were found for all electrical current intensities applied to the tribological contact, regardless of the lubrication regime.

The aim of the current study is to answer some important questions that have been overlooked by the previous research: (I) as the current passage transforms the tribological contact into an anode and cathode, how does this affect the contact interacting with the additives and tribofilm formation? (II) what is the dielectric response of the lubricant to the passage of current in the boundary lubrication regime? (III) how does the current density affect the wear, failure mechanisms and WEC initiation? and (IV) what are the measured current attributes (intensity and voltage) inside the tribological contact and the calculated current density (current intensity in the tribological contact divided by the Hertzian contact area) in the RCF testing? The study employed a commercial gearbox oil tested in MTM and MPR tribometers (PCS Instruments) where the tribological contacts were connected to an electrical setup. The tests were carried out with the MTM Ball and MPR Roller as cathodes (negatively charged).

2. Experimental methods

2.1. Test rigs and conditions

Tribological tests were conducted using the Mini Traction Machine (MTM-SLIM) and Micro Pitting Rig (MPR) supplied by PCS Instruments. The test conditions are summarised in Tables 1 and 2. The two tribometers were ideally suited to study the role of electrical contact on tribofilm formation (MTM-SLIM) and RCF life and evolution of wear mechanisms (MPR).

Tribofilm formation was investigated in the MTM using a three steps test routine alternating at fixed time intervals. Firstly, a 'conditioning phase' is undertaken when the ball is rubbed against the disc surface in boundary lubrication conditions to generate a tribofilm on ball and disc wear tracks. This step is followed by the 'Stribeck curve' acquisition, when the friction is measured over a range of rolling speed at a fixed Slide to roll ratio, SRR, starting from higher and progressing to lower speeds. The third step was the 'tribofilm measurement' using the SLIM attachment, when the stationary ball is loaded against the spacer layer-coated window to capture an image of the ball wear track.

The testing was carried out in boundary lubrication and a negative SRR was chosen as it has been shown to be a driver in WEC formation [44]. In the MPR this means that the central roller moves faster than the rings and the combination of rolling speed (3.4 m/s) with SRR leads to a linear speed of 2.89 m/s for the rings (1022 rpm) and 3.91 m/s for the roller (6223 rpm). As such, the roller experiences 1.12 million contact cycles per hour. The occurrence of surface damage on wear tracks increases the roller vibration level, measured using an accelerometer. The trip condition for CLA acceleration was set as 5 g and for the Peak-to-peak acceleration was 15 g. Tests were concluded when either the time condition was reached (288 h, which results in 322 million contact cycles), or when the trip condition for roller vibration was exceeded.

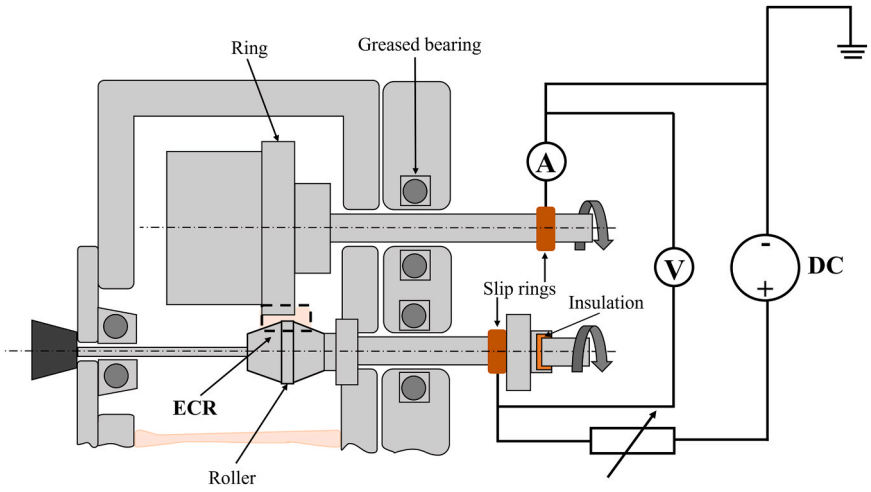

Fig. 2. Schematic representation of the electrical circuit setup connected to MPR.

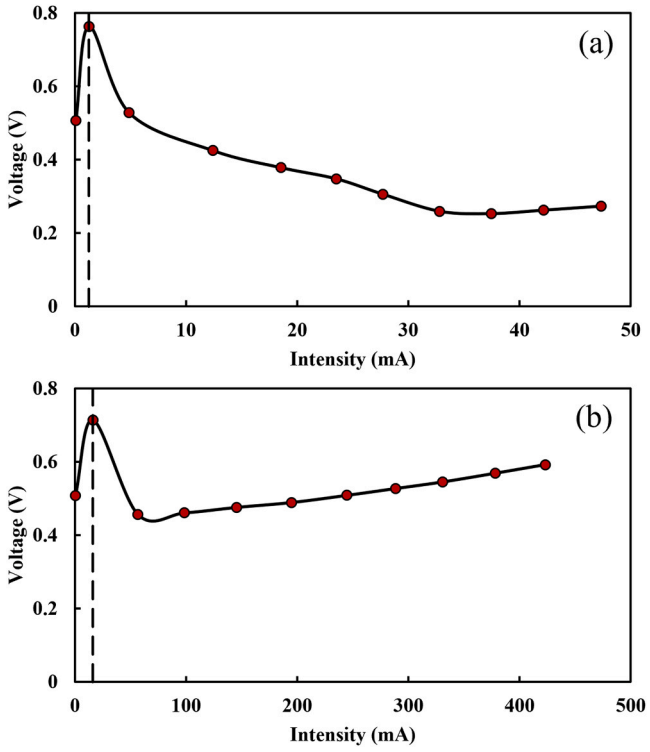

Fig. 3. I-V plots measured in MTM electrical setup with the gearbox lubricant at 100 Ω **(a)** and 10 Ω **(b)** applied from the variable resistor. With dashed line is separated capacitor behaviour (before breakdown point) and Ohmic resistor behaviour (after breakdown point) of the lubricant.

The MTM and MPR specimens were supplied by PCS Instruments and made of AISI 52100 through hardened steel. The 19.05 mm MTM ball and 46 mm MTM disc each had a Rq roughness of 11 ± 3 nm and composite roughness of approximately 16 nm. In the MPR, a crowned 12 mm roller with 1 mm wide wear track contacts three counter rings with a diameter of 54.15 mm. The Rq roughness of MPR roller and rings was 0.1 μm, and the composite roughness was approximately 0.14 μm.

Each test was conducted with a new ball/disc pair and roller/rings that had been ultrasonically cleaned with a hydrocarbon-mix solvent (FASTCLEAN 201, CRC Industries UK Ltd) and isopropanol prior to the test.

The tests were run in a gearbox lubricant, which has a relative

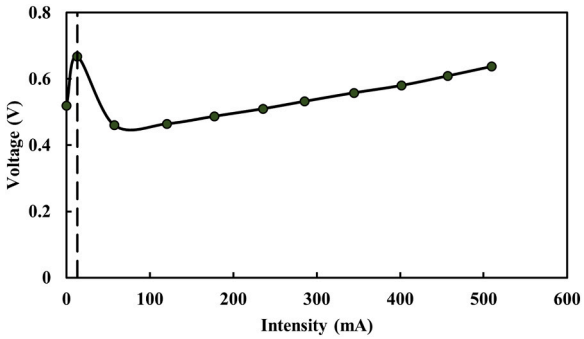

Fig. 4. I-V plot measured in MPR electrical setup with the gearbox lubricant. With dashed line is separated capacitor behaviour (before breakdown point) and Ohmic resistor behaviour (after breakdown point) of the lubricant.

density of 0.867 g/cm^3 a kinematic viscosity of 63.26 cSt at 40 °C and 11.43 cSt at 100 °C, and a pressure-viscosity coefficient (α) of 9.83 GPa^{-1}.

The electrified tests were carried out by connecting the MTM and MPR tribometers to an electrical circuit consisting of a DC power supply, a variable resistor and a multimeter (Fig. 1 **and** Fig. 2). To apply positive/negative voltage, two channels of the DC power supply were connected in series which allows for a specific electrical polarisation (cathodic/anodic) of the tribological specimens to be selected. A digital multimeter was employed to measure the intensity and voltage values across the tribological contact. The MTM specimen connection with the electrical circuit was provided from the ball shaft (which is grounded) through copper slip ring and brushes and a Mercotac bushless slip ring on the MTM disc shaft. The MPR tribological contact was connected to the electrical circuit by two copper slip rings installed on the roller and upper ring shafts and carbon brushes. The ring shaft is grounded, and the roller shaft is insulated as shown in Fig. 2.

To understand the lubricant behaviour in the electrified/charged tribological contact operating under boundary lubrication, a preliminary study was carried out in each of the two tribometers.

I-V curves were measured to study the breakdown voltage of the lubricant film by applying for 30 seconds an external voltage between 0 and 5 V, in steps of 0.5 V. The tribological and electrical test conditions used in this study are summarised in Table 1 (MTM-SLIM) and Table 2 (MPR). After the breakdown curves were measured in the MTM and MPR, the tribofilm formation (in MTM) and RCF (in MPR) tests were carried out at applied voltages above that at which the breakdown of the lubricant occurs (Fig. 3 **and** Fig. 4**)**.

The tribological tests were carried out with the MTM Ball and MPR

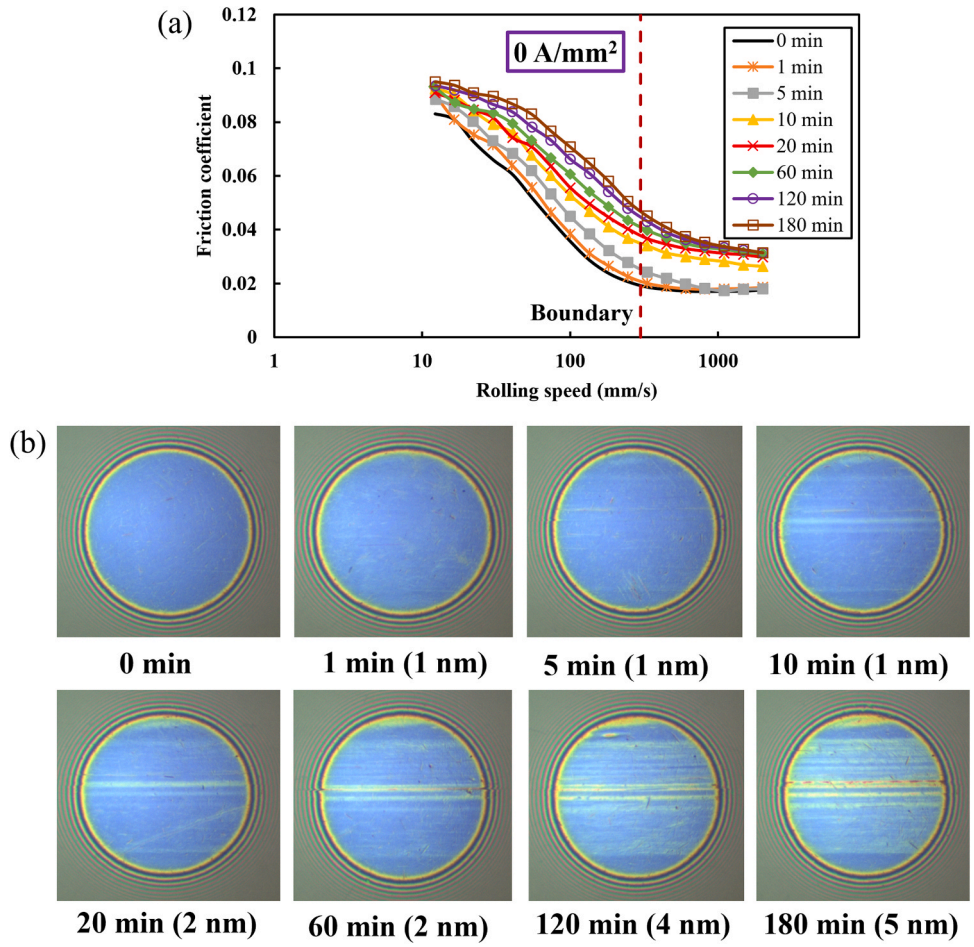

Fig. 5. MTM results measured after 0, 1, 5, 10, 20, 60, 120, and 180 minutes of testing at 100°C with 0 A/mm^2 at the contact (a) Stribeck curves, (b) SLIM interferometry images of the ball wear track.

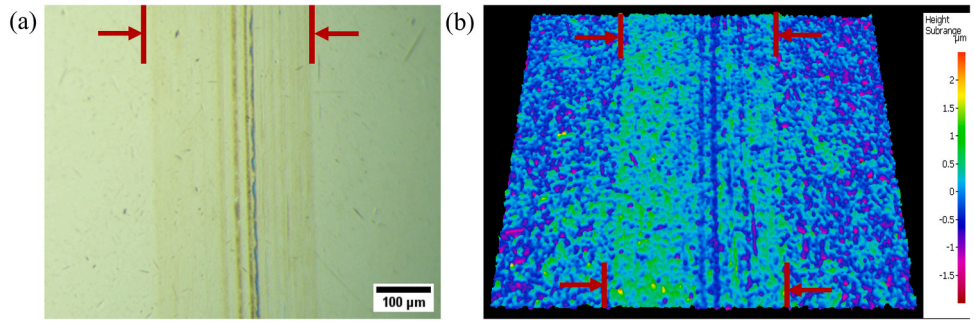

Fig. 6. Images of the tribofilm on the MTM ball after 3 h conditioning time. The red arrows indicate the wear track. (a) Optical image of the wear track, (b) Alicona 3D map of the tribofilm.

Roller as cathodes (negatively charged).

2.2. Surface analyses

The morphology and composition of the wear tracks of the MTM and MPR specimen were analysed by optical microscopy (Olympus BX41M-led), SEM/EDX (JSM-7200FSchottky Field Emission SEM) and profilometry (Stylus and Alicona Infinite).

2.3. Roller metallographic preparation

To investigate the presence of WECs, all rollers employed in the RCF tests were sectioned transversely to the wear track and then longitudinally to the wear track using a precision sectioning saw. Roller sections were mounted in Bakelite, ground and polished using 120, 800, 1200 and 4000 grit grinding sheets, followed by polishing with 3 µm, 1 µm and 1/4 µm polishing clothes. The mounted samples were then etched with 2 % Nital (2 % nitric acid in ethanol). The etched samples were examined for microstructural alterations by optical microscopy and SEM.

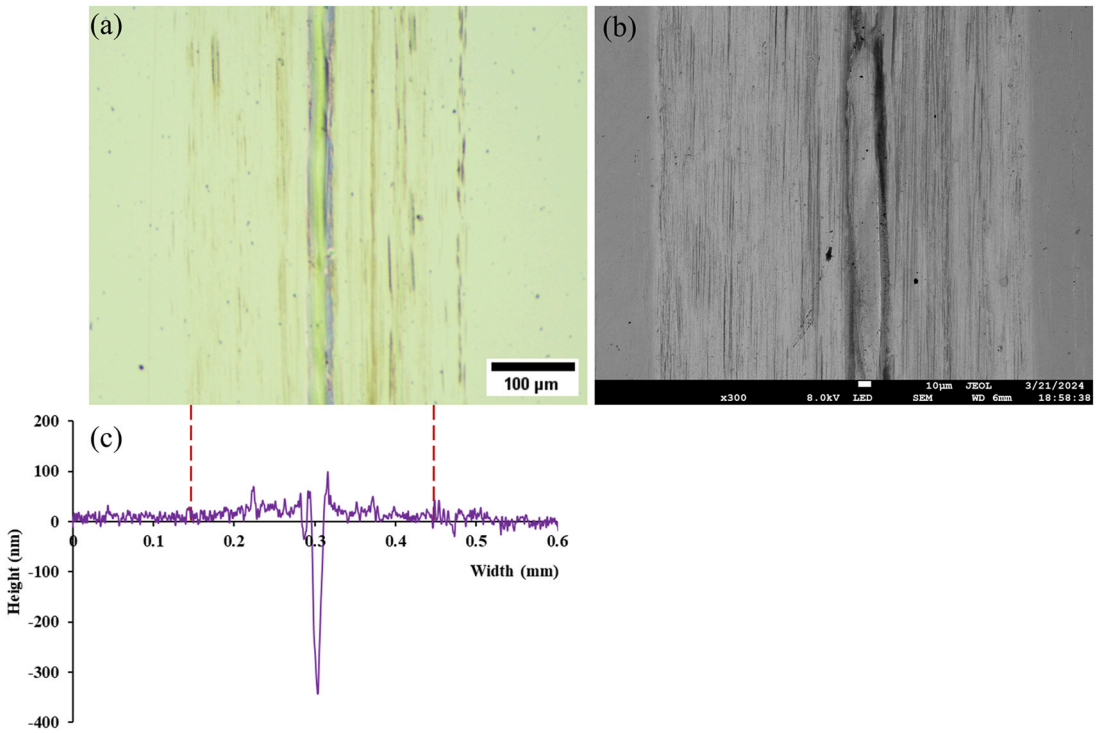

Fig. 7. Images of the wear track and tribofilm on the MTM disc after 3 h conditioning time. (a) Optical image, (b) SEM image (c) roughness profile measured across the wear track with Stylus profilometer.

Table 3
Average tribofilm thickness on MTM ball (measured by SLIM) and disc (Stylus profilometer).

	Average tribofilm thickness and standard deviation (nm)
Ball (SLIM)	4 ± 1.4
Disc (Stylus profilometer)	9.6 ± 5.7

Table 4
Parameters used to calculate the completed distance for the ball and disc specimens.

	Ball	Disc
Diameter (mm)	19.05	46
Wear track diameter (mm)	17.34	42
Circumference (mm)	54.44	131.9
Linear speed (mm/s)	115	85
Rotational speed (cycles/minute)	115.3	38.7
Completed distance (mm/minute)	6276.9	5104.5

3. Results and discussion

3.1. The effect of electrical current on lubricant behaviour

As discussed in 2.1, to understand the lubricant dielectric behaviour in an electrified tribological contact as a function of the external voltage applied, a preliminary electrical study was carried out on the MTM and MPR lubricated contacts operating in boundary conditions, as employed in the tribological testing. The I-V curves measured with a multimeter across the tribological contact when the applied external voltage was increased from 0 to 5 V in steps of 0.5 V, reveal that the lubricant behaviour markedly depends on the voltage value applied and most importantly, inform which applied voltage values/range preserve the lubricant dielectric property (to prevent or rapidly quench electric discharges).

The characteristic I-V curves for the investigated oil in the MTM and MPR electrified tribological contacts are depicted in Figs. 3 and 4. Both I-V curves present four distinct zones: (1) an *Increased resistance* zone, where the lubricant behaves as a resistor and prevents current leakage through the specimens; (2) a *Breakdown* zone, where the breakdown strength/voltage of the lubricant is exceeded; (3) a *Decreased resistance* zone, where the current starts to flow across the tribological contact and the lubricant resistance decreases; (4) a Constant resistance zone, where the lubricant behaves as an Ohmic conductor. Two values of external variable resistance were used in the MTM electrical setup to determine the breakdown strength of the oil. With a variable resistor value of 100 Ω, the breakdown strength is 0.76 V (Fig. 3**.a**) and with a resistor of 10 Ω, the breakdown strength is 0.71 V (Fig. 3**.b**). The breakdown voltage decreases when the external resistance (variable resistor) decreases.

The I-V curve measured in the lubricated MPR electrical setup with a balance resistance of 5 Ω has a breakdown voltage of 0.67 V (Fig. 4).

The lubricant breakdown strength values (current and voltage) measured in MTM and MPR contacts and their corresponding applied/external voltage values inform the selection of the external voltage used during the tribological testing. During the tribological testing, applied voltages higher than that corresponding to the lubricant breakdown strength were employed. The corresponding current values from the I-V curve were then divided by the Hertzian contact area to calculate the current density in the tribological contact. To enable the correlation of the results from the MTM and MPR, similar current density values were used during the tribological testing.

Three steps were followed to determine the values of electrical parameters employed in the MTM and MPR testing:

1. I-V curves are measured in MTM and MPR in boundary lubrication by applying external voltages in the range 0–5 V
2. **applied** voltages higher than that corresponding to the breakdown strength (values from the "**constant resistance**" zone on the I-V breakdown curve) were used for tribological testing

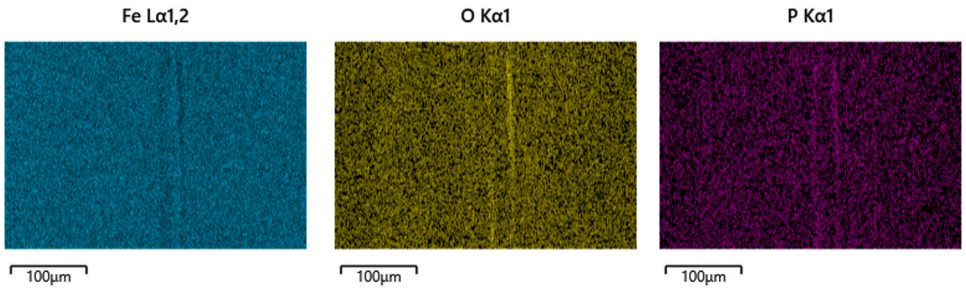

Fig. 8. EDS analysis of the disc wear track after 3 h of rubbing.

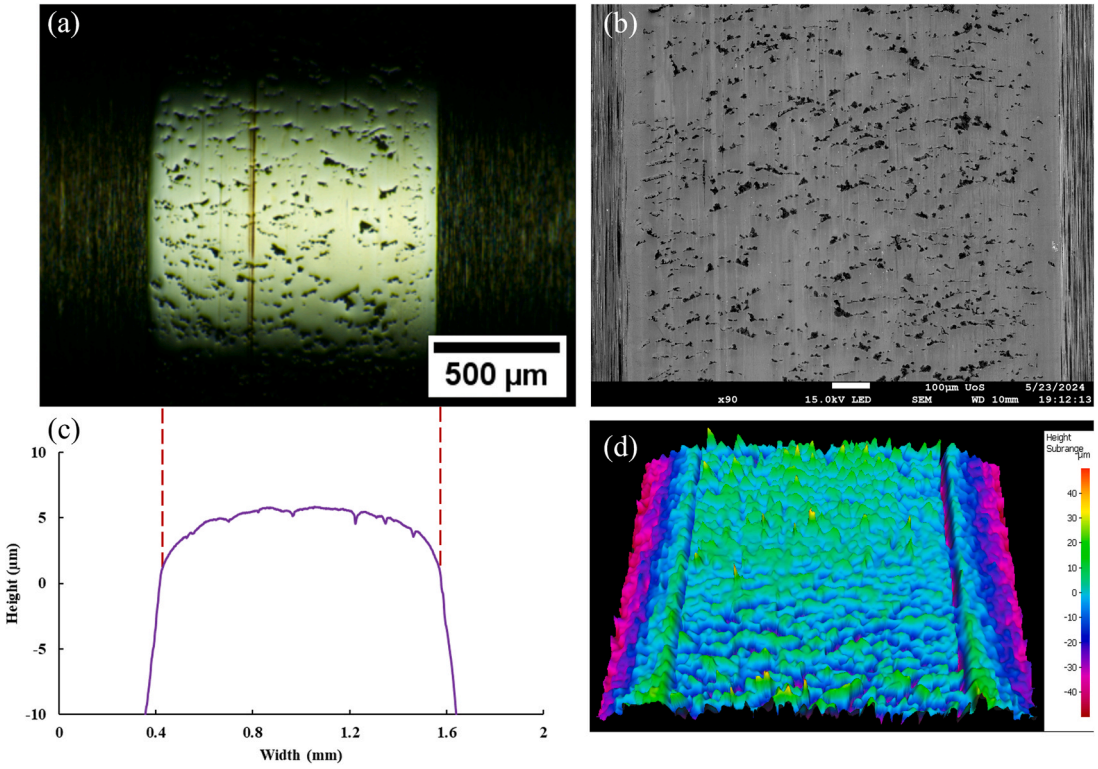

Fig. 9. MPR Roller wear track after 288 h/ 322 million contact cycles: (a) Optical image, (b) SEM-EDS image, (c) Stylus profile, and (d) Alicona 3D map.

Table 5
Elemental composition of the tribofilm.

Element	Fe	Cr	O	Mn	C	P	S
mass %	95.14	1.68	1.34	0.52	0.50	0.28	0.15

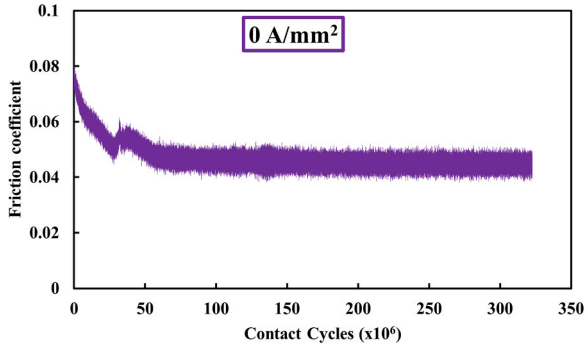

Fig. 10. COF during the 288 hours test in MPR tribometer.

3. the measured intensity values corresponding to the **applied** voltage were taken from the breakdown curve
4. similar current densities are used for the MTM and MPR testing (the current intensity divided by Hertzian contact area).

3.2. *Tribofilm growth and wear evolution in 'No applied electrical field'*

3.2.1. *Characteristics of the tribofilm generated by lubricant*

Fig. 5 **(a)** shows the Stribeck curves for the lubricant at 100°C in 'No applied electrical field', illustrating the friction properties of the tribofilm at different stages of formation during the rubbing stage of the testing. The lubricant shows a friction coefficient that increases gradually over time in the boundary and mixed lubrication regimes (based on the present study testing conditions, the calculated values for the specific film thickness λ of ~3 and ~1 corresponded to the 1400 mm/s and 300 mm/s, respectively). A significant increase in friction started after 10 minutes of rubbing and then gradually continued until the end of testing. These results depict the kinetics of tribofilm growth/removal over time. Fig. 5 **(b)** shows the corresponding SLIM (optical interference) images of the tribofilm on the ball wear track. The first SLIM image was taken before the start of the test and the interference colour

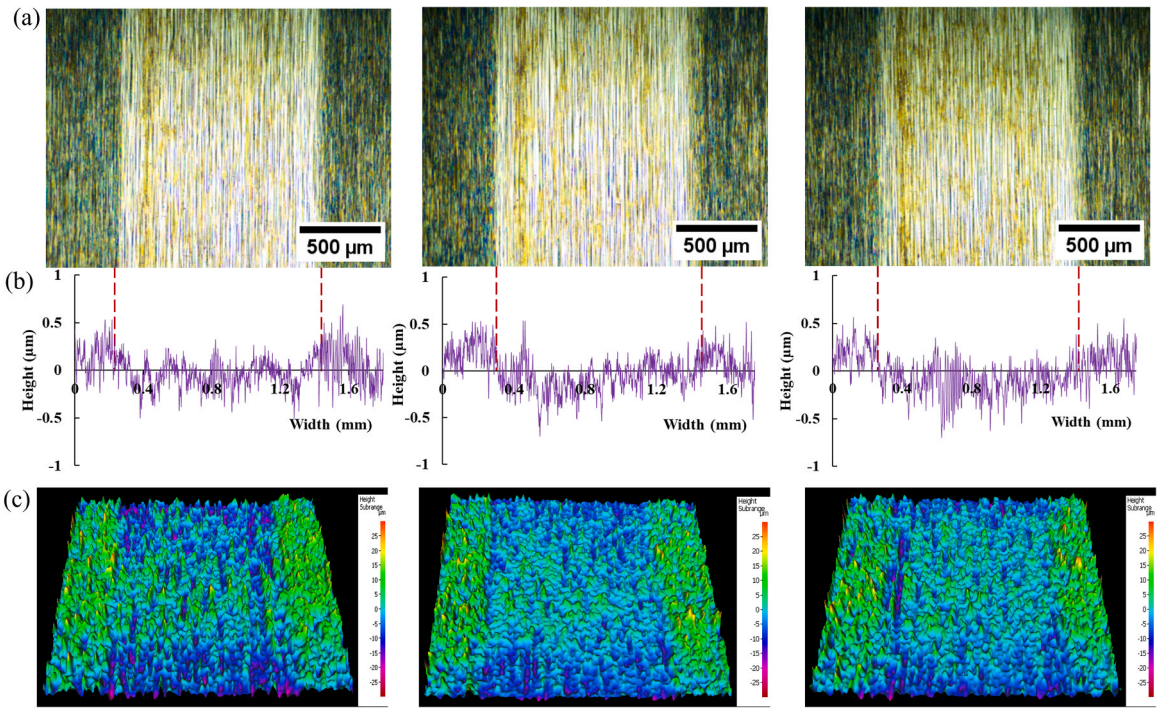

Fig. 11. Wear tracks on the three MPR rings after 288 h/ 322 million contact cycles (a) Optical images (b) Stylus wear profiles measured across the wear track, (c) Alicona 3D maps.

Table 6
Width of the wear tracks on the MPR roller and rings.

Specimen	Roller	Ring 1	Ring 2	Ring 3
Width (µm) ± SD	1149.2 ± 12.6	1213.0.9 ± 12.1	1218.4 ± 6.9	1215.4 ± 6.7

indicates that there is no film present. However, as rubbing in boundary lubrication conditions takes place, a streak-like solid film is visible after 10 minutes of rubbing with a higher density at the centre of the contact, where the pressure is greater. This gradually becomes thicker and more uniform. The increase in film thickness and roughness/uneven distribution can be correlated with the increase in friction depicted by the Stribeck curves. As the test progressed, the boundary lubrication COF increased steadily from 0.095 (0 minute) to 0.1 (180 minutes).

These results indicate that the tribofilm has slow growth kinetics and the final thickness after 180 minutes of rubbing was only 5 nm. It is thought that the thin tribofilm is the product of the anti-wear additive and friction modifier which compete for absorption/reaction on the wear track and, thereby, impede the generation of thick anti-wear films. Similar results have been reported by Ref. [45].

Fig. 6 presents the optical image of the ball wear track and the Alicona 3D image of the tribofilm on the ball. Both optical image and Alicona 3D map show a thin, streak-like tribofilm and agree with the 3D SLIM interferometry image.

The optical and SEM images of the disc wear track (Fig. 7) reveal a thin streak-like tribofilm with a groove at the centre of the contact, confirmed by the roughness profile measured across the wear track. Table 3 **shows** the average height of the tribofilm on the discs and balls from repeat tests. **The average tribofilm on the disc** was calculated from multiple wear track profiles measured at positions 0, 90°, 180°, and 270° while on the ball this was obtained from the SLIM interference images at the central region.

The calculated average thickness of the tribofilm measured by the Stylus profilometer on the MTM discs is greater than that on the MTM balls measured by SLIM interferometry. This difference in the tribofilm thickness can be explained by two factors. Firstly, the SRR has a direct impact on tribofilm growth and the final tribofilm thickness is a result of the balance between its formation rate (associated with the kinetics of

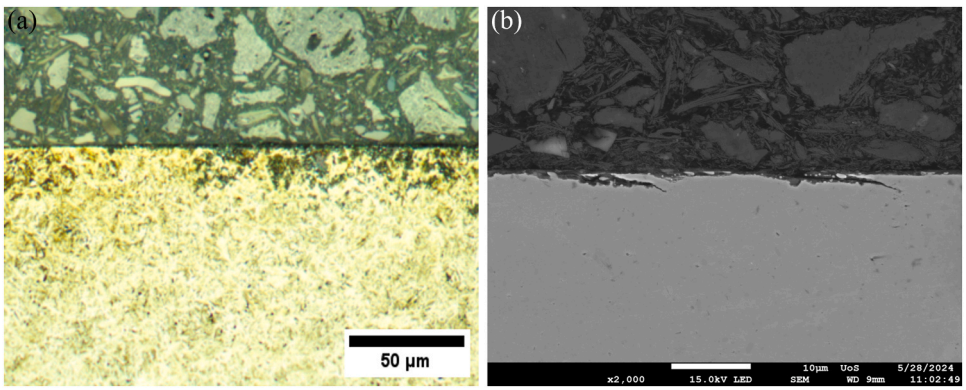

Fig. 12. Optical image of the etched microstructure **(a)** and SEM image of fatigue cracks initiating from the surface **(b)**.

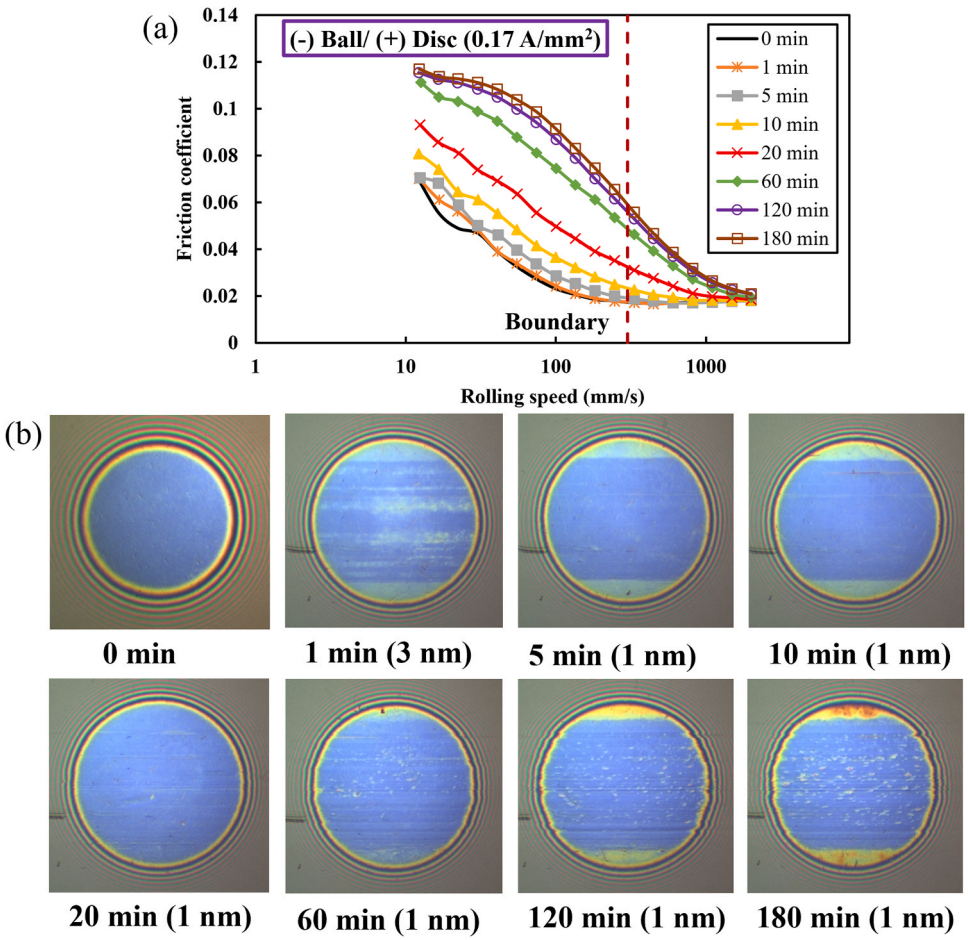

Fig. 13. MTM results measured after 0, 1, 5, 10, 20, 60, 120, and 180 minutes of testing at 100°C with 0.17 A/mm^2 at the contact (a) Stribeck curves, (b) SLIM interferometry images of the ball wear track.

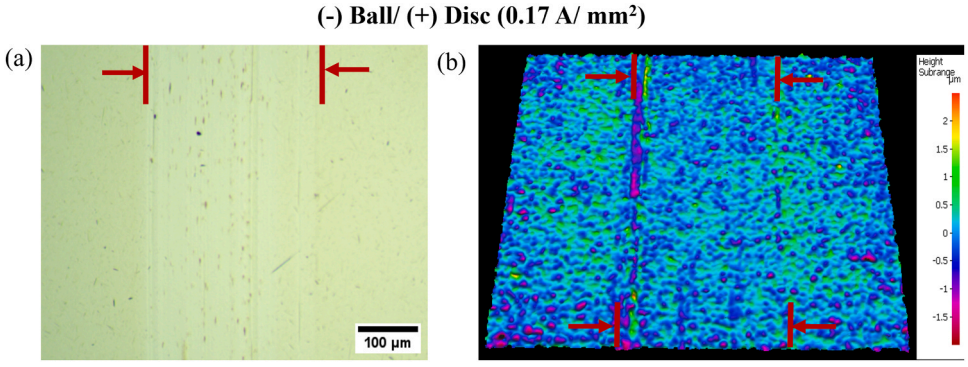

Fig. 14. Images of the tribofilm generated on the wear track of the MTM ball after 3 h conditioning time. (a) Optical image, (b) Alicona 3D map. The red arrows indicate the wear track.

chemical reactions) and its removal rate (associated with wear processes). The current study used a −30 % SRR and a mean speed of 200 mm/s, which results in a speed of 115 mm/s for the ball and 85 mm/s for the disc. As shown in Table 4, the difference of speeds and diameters of ball and disc specimens leads to a different distance completed during the test, which can affect the tribofilm thickness. Table 4 shows the parameters used to calculate the completed distance for the ball and disc specimens.

Thus, the ball completed a distance greater by a factor of ~1.2 than the disc, which can result in higher wear and thinner tribofilm on the ball than on the disc. Secondly, the tribofilm on the ball is measured by SLIM interferometry *in-situ* under the testing pressure (50 N) which results in a flattening of the tip asperities and thus a smaller film thickness.

The elemental composition of the tribofilm generated after 3 hours of rubbing on the disc was analysed by SEM-EDX mapping and shown in Fig. 8. As expected, phosphorus and oxygen from the anti-wear additive, was detected in the central part of the wear track and at the edges of the groove in the tribofilm.

3.2.2. *Wear mechanisms in RCF tests and their evolution*

In the absence of an applied electrical field, the RCF tests in the MPR ran for the entire test procedure (322 million cycles) without failing.

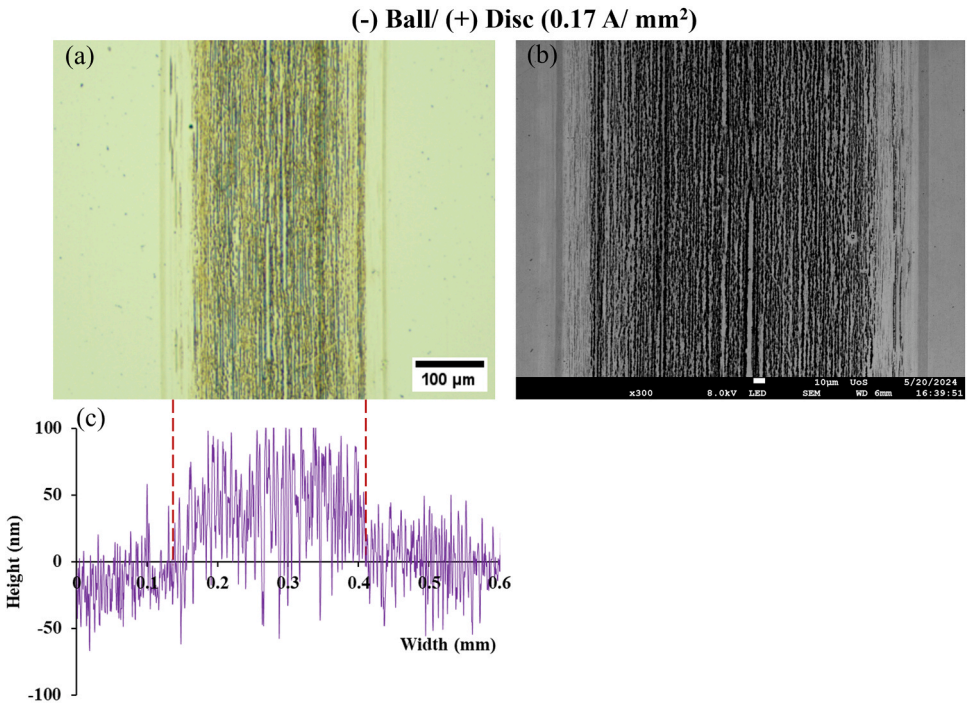

Fig. 15. Wear track on MTM disc after 3 h of rubbing (a) Optical image of the tribofilm, (b) SEM image of the tribofilm, (c) Stylus wear profiles measured across the wear track.

Table 7
Average film thickness measured on the MTM ball (using SLIM) and MTM disc (Stylus profilometer).

	Average tribofilm thickness and standard deviation (nm)
Ball (SLIM)	1
Disc (Stylus profilometer)	31.7 ± 5.9

Fig. 9 shows post-test analysis on the roller wear track by optical microscopy, SEM, contact and optical profilometry.

All of them reveal micro-pits evenly distributed over the roller wear track and a thin layer of tribofilm covering the outermost surface. Micro-pitting is a wear mechanism associated with contact fatigue failure, which is initiated by micro-cracks normal to the sliding direction, whose propagation results in micro-pit formation. The diameter of the micro-pits is in the 10 – 30 µm range and their depth 5 – 10 µm. It is thought that the micro-pitting mechanism is influenced by factors such as surface roughness, microstructure, residual stresses, lubricant composition, and operating conditions. The evolution of the micro-pitting wear mechanism results in an increase in noise and vibration levels and can lead to more severe damage such as macro-pitting and spalling [46,47].

The EDS elemental composition (mass%) of the wear track is presented in Table 5. The elements O, P, S, and C were identified in the tribofilm. Fe, Cr, and Mn are present in AISI 52100 steel alloy composition and they are not usually present in lubricants.

The change to the width of the roller track during RCF testing was recorded by taking optical images before and after the test (after 322 million contact cycles) at multiple positions (0°, 90°, 180° and 270°). To understand the effect of thermal energy from friction on wear, optical images of the roller track were processed with ImageJ software, and an increase in the width of wear track by approximately 100 µm from 1051.8 ± 19.7 µm to 1149.2 ± 12.6 µm, was noticed during the test. This can be explained by the thermal expansion dilatation of the rubbing surfaces resulting from prolongated frictional heating and wear.

The COF evolution during the test is depicted in Fig. 10. As the testing was run in the boundary regime and the MPR specimens have high roughness (R_q 0.1 µm), in the early stages of testing the value of COF was higher at 0.08, but after 50 million contact cycles the COF stabilized at 0.05 and then remained constant for the rest of the test.

The end of test wear tracks on the three MPR rings used as counter bodies (in contact with the roller) are shown in Fig. 11. The top row (a) displays the optical images, the middle row (b) the profiles measured by the contact profilometer and the bottom row (c) the 3D maps. Both, the

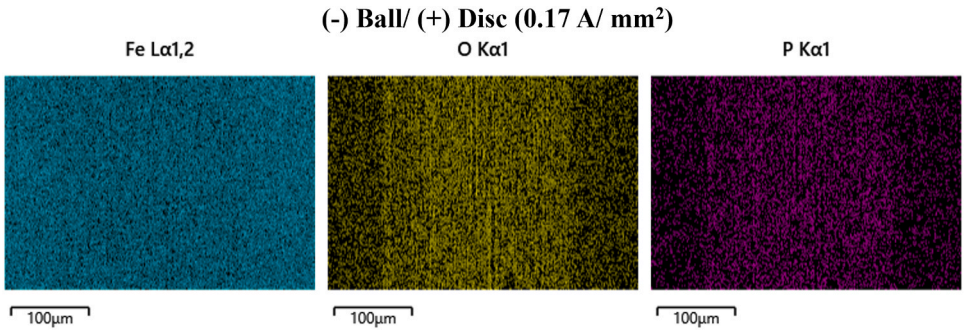

Fig. 16. EDS elemental distribution on the disc wear track after 3 h of rubbing in (-) Ball/ (+) Disc configuration and 0.17 A/mm^2.

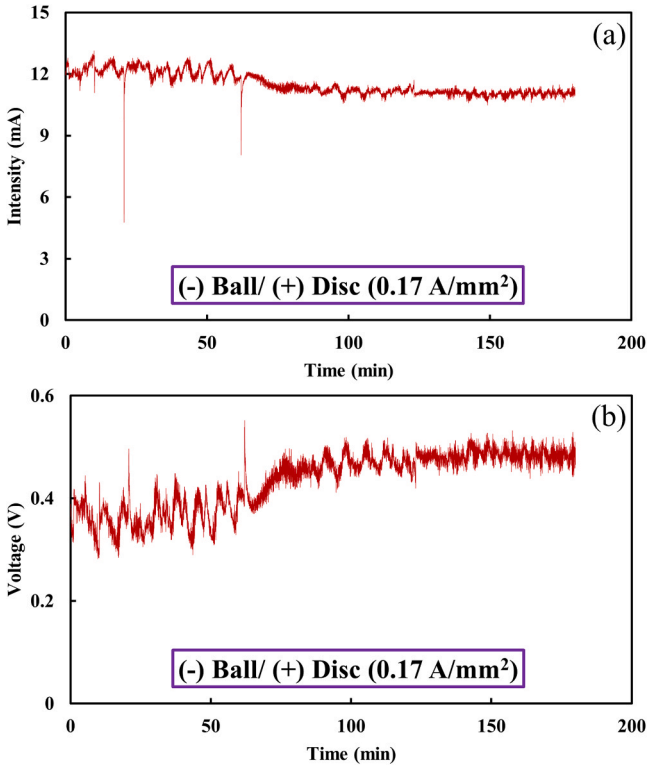

Fig. 17. Electrical parameters measured with the electrical setup during the 3 h test with (-) Ball/ (+) Disc configuration and 0.17 A/mm^2 across the MTM tribological contact: (a) Intensity and (b) Voltage.

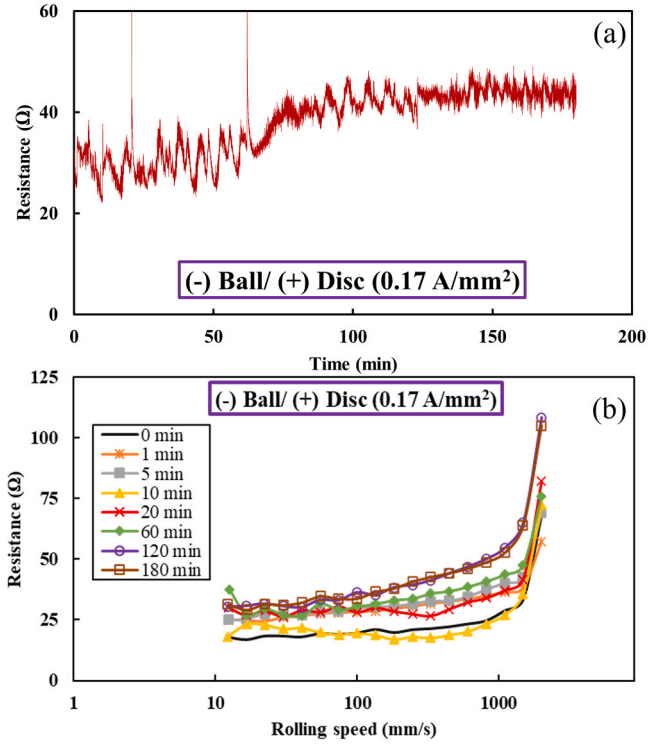

Fig. 18. Resistance measured in MTM tribological contact with (-) Ball/ (+) Disc configuration and 0.17 A/mm^2 current density (a) Resistance across the contact (b) Resistance vs rolling speed/film thickness after 0, 1, 5, 10, 20, 60, 120, and 180 minutes of testing.

Table 8
Average values for intensity, voltage, and resistance in MTM contact during the 'conditioning phase'.

	Mean values and standard deviation
Intensity (mA)	11.9 ± 0.5
Voltage (V)	0.39 ± 0.05
Resistance (Ω)	33.1 ± 5.4

contact and optical profiles show wear induced material loss of about 0.9 μm depth at the area of contact between rings and roller. The surface wear leads to the removal of the rough asperities during the RCF test. The decrease in surface roughness is in agreement with the diminution of the COF.

The average values of the width of the wear tracks measured with the ImageJ software are shown in Table 6.

Following the investigation of the roller wear track surface, the sub-surface was checked for damage. Fig. 12 presents an optical and a SEM image of the region beneath the roller wear track after metallographic preparation. The optical image shows the AISI 52100 microstructure after etching with 2 % Nital and the absence of WECs. The SEM image shows small fatigue cracks initiating at the surface.

3.3. Tribofilm growth and wear evolution in the Ball/ Roller cathode configuration

As explained in 3.1, the lubricant breakdown curves in the MTM and MPR contacts were used to select the applied voltage value for the tribological tests. The applied voltage value used for testing was higher than that producing the breakdown of the lubricant.

3.3.1. Effect of low current density across the tribological contact

A similar investigation of friction, wear and tribofilm formation to that described in **3.2** was undertaken for electrified MTM and MPR contacts.

3.3.1.1. Characteristics of the tribofilm generated by lubricant. MTM tribological tests were performed with + 1.6 V from the DC power supply and 100 Ω from the external resistor. These conditions result in a positive voltage on the disc and a negative voltage on the ball, a current density of 0.17 A/mm^2 across the tribological contact and lubricant breakdown.

Fig. 13 illustrates the Stribeck curves for lubricant and the corresponding SLIM images. As the SLIM images show, no tribofilm is formed on the wear track when the ball functions as a cathode but on some images a film seems to be present outside the wear track. The film outside the wear track can be an absorbed layer without strong chemical bonding to the substrate. After the balls had been gently wiped prior to their wear track analysis, the absorbed/reacted layer on the sides of the wear track was not observed (Fig. 14).

Despite the SLIM images not showing tribofilm formation on the ball, the gradual friction increases with time observed on the Stribeck curves indicates that a tribofilm was continuously generated in the contact during testing, probably on the disc wear track. Most of the increase took place between 10 and 60 minutes of rubbing. The morphology of the tribofilm evolved and after 120 minutes the Stribeck curves became smoother and more uniform (Fig. 15). The COF in the boundary lubrication regime was 0.076 at the beginning of the test and 0.117 at the end. Higher values of COF at the end of the test were measured for the electrified test than for the 'No applied electrical field' test.

The optical image of the ball wear track is in agreement with the SLIM interferometry images (Fig. 14) and shows that the tribofilm on the ball wear track is almost absent with the exception of a few micrometre-sized spots at the centre. The 3D map reveals that the inside track is smoother than the outside and the presence of a superficial scratch on the left edge.

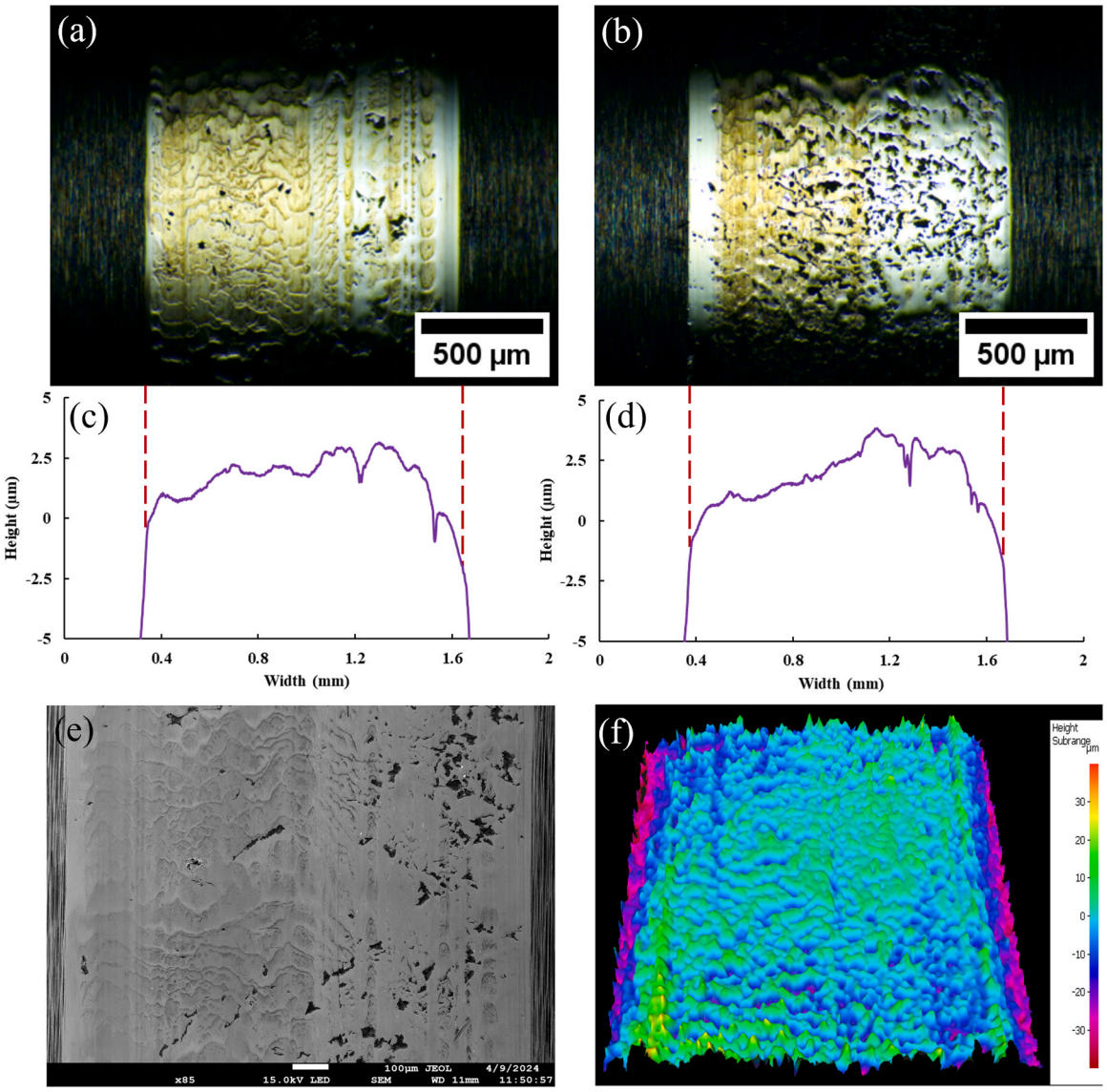

Fig. 19. MPR Roller wear track after 288 h/ 322 million contact cycles in (-) Roller/ (+) Ring configuration and 0.19 A/mm^2 across the tribological contact: (a) optical image, (b) SEM image, (c) Stylus profilometry, and (d) Alicona 3D map.

Optical and SEM images along with the profile of the disc wear track are shown in Fig. 15**.** As expected, the anode (+) disc attracts the organic anion moieties of the lubricant additives (carboxylates, phosphates, sulfonates etc.) and forms the tribofilm. Both, optical and SEM images reveal that the disc wear track is covered by a smooth, uniform 31.7 nm thick tribofilm. Compared with the tests in the 'No applied electrical field' configuration, where the tribofilm formed on both ball and disc specimens at different rates, in the case of the (-) Ball/ (+) Disc the tribofilm formed exclusively on the disc and is thicker as revealed by the wear track profile.

The mean tribofilm thickness values on the disc were calculated from multiple track profiles and discs from repeat tests. Similarly, the mean values of the thickness of the tribofilm on the ball wear track were calculated from different samples using SLIM software and are listed in Table 7.

Fig. 16 presents the SEM-EDS mapping of iron, oxygen and phosphorus on the disc wear track which indicates that the steel substrate is completely covered by a phosphorus and oxygen (phosphates/phosphonates) rich tribofilm. The concentration of these elements is higher than on the 'No applied electrical field' wear track which implies a thicker and more uniform tribofilm is generated on the positively charged (anode) disc.

Fig. 17 illustrates the electrical parameters (intensity and voltage) measured across the tribological contact using the electrical setup during the 'conditioning stage' of the testing. The intensity curve fluctuates but gradually decreases during the first 60 minutes of testing and is followed by levelling up towards the end of testing. The voltage, as an inverse function of current intensity, shows opposite behaviour with the voltage increasing and fluctuating in the first 60 minutes of testing and levelling out afterwards. Ohm's law was applied to calculate the resistance variation during the 'conditioning stage' (Fig. 18**.a**) and 'Stribeck curves stage' (at 0, 1, 5, 10, 20, 60, 120, and 180 minutes plotted against the rolling speed at which they were measured) (Fig. 18**.b**). Each mean resistance value was calculated from 6 intensity and voltage values taken every minute during the two stages. The 'conditioning stage' resistance graph in Fig. 18**.a** demonstrates that in the first 60 minutes of testing where tribofilm growth-removal takes place, the resistance fluctuates and subsequently, an increase in resistance across the tribological contact is noted which levels out afterwards. A higher resistance measured in the contact can be related to the generation of a thicker

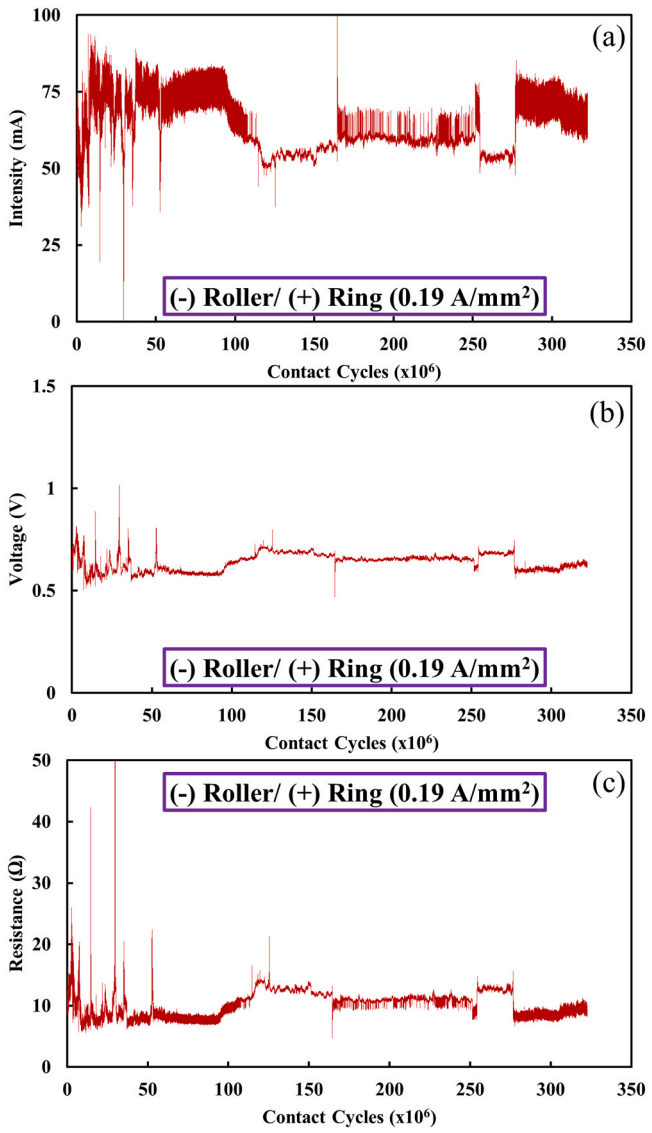

Fig. 20. Electrical parameters measured across the MPR tribological contact for (-) Roller/ (+) Ring configuration and 0.19 A/mm^2 (a) intensity, (b) voltage and (c) calculated resistance.

Table 9
Average values for measured intensity and voltage, and calculated resistance in MPR contact.

	Mean values and standard deviation
Intensity (mA)	63.2 ± 8.7
Voltage (V)	0.64 ± 0.04
Resistance (Ω)	10.5 ± 16.1

Table 10
Elemental and mass% composition of the tribofilm from SEM/EDX.

Element	Fe	Cr	O	Mn	C	P	S	N
mass %	91.68	1.62	2.16	0.56	0.81	1.71	0.08	0.9

tribofilm. The mean values for measured intensity and voltage across the MTM tribological contact and the calculated resistance are presented in Table 8.

The 'Resistance Stribeck curves' (resistance versus speed) in Fig. 18**b** show an expected increase of resistance with rolling speed/lubricant film thickness, and also with the rubbing time. The variation of resistance with time of these curves is in good agreement with the resistance variation in Fig. 18**.a** e.g.in the first 60 minutes of testing, the curves show fluctuations (increases and decreases), and later the resistance values stabilise. The increase of the lubricant film thickness separating the surfaces at speeds > 1.5 m/s dramatically increases the contact resistance.

3.3.1.2. Wear mechanism and its evolution. Rolling contact fatigue tests with an applied electrical field were performed with the MPR fitted with electrical setup. A voltage of –1 V from the power supply resulted in a negative (cathode) roller and positive (anode) ring. The external resistor value was 5 Ω. These conditions lead to the breakdown of the oil film (zone 2 in Fig. 4) and a current density of 0.19 A/mm^2 across the tribological contact which was approximately the same as in the MTM. In this testing configuration, the test ran for 288 hours/ 322 million contact cycles without failing.

The optical and SEM images, profile and 3D map of the post-test roller wear track (Fig. 19) reveal two competing wear mechanisms: micro-pitting and wavelets (a novel wear mechanism that has not been reported in the literature to date which consist of surface features with peaks and valleys orientated perpendicular to the sliding direction). The evolution of these wear mechanisms was studied by optical microscopy and SEM-EDS analysis over time intervals of 1 hour, in first 3 hours, and intervals of 3 hours afterwords. The investigation revealed that the micro-pitting mechanism occurred after approximately one hour, whilst the first sign of wavelets appears after about 15 hours of testing. As the test progressed in time, three distinct zones emerged on the wear track: (1) wavelets zones; (2) micro-pitting zones; and (3) zones containing both, micro-pitting and wavelets. A possible cause of wavelet formation can be the combination of factors such as energy released from frictional and Joule heating. The frictional heating caused by the 1.12 million contact cycles/ hour and Joule heating from the passage of electrical current can soften the material of the roller wear track and generate wavelets. The sliding direction determines the orientation of the wavelets.

The measured intensity and voltage values across the contact and the calculated contact resistance values during the testing are plotted against contact cycles in Fig. 20. The intensity curve reveals three distinct regions, two of high and one of low values. The two zones with the high current intensity were measured in the first ~100 million contact cycles (~89 hours) and in the last ~ 50 million contact cycles (~45 hours), with a lower current intensity zone recorded in between. The contact resistance curve shows low values in the first ~100 million contact cycles and the last ~ 50 million contact cycles, and a higher resistance in between. The first low resistance zone can relate to tribofilm growth similar to that measured in the MTM electrical setup. The decrease in resistance can be related to tribofilm removal and surface damage. The mean values and standard deviation for intensity, voltage and resistance are presented in Table 9.

The EDS elemental composition in mass percentage of the wear track is presented in Table 10. The valley in the zone with wavelets are covered by a tribofilm rich in P, O (originating from the anti-wear additive) and C (from the base oil). In addition, N was identified in the pits and may be related to the antioxidant additive. The presence of N on the (-) Roller is due to the ability of the amine to dissociate in positively charged moieties and migrate to the roller.

Analysis was also carried out on the three rings used as counter bodies in the MPR tests with (-) Roller/ (+) Ring. Ring 1 is connected to the electrical circuit and is positively polarised, which means it acts as anode. Rings 2 and 3 were not connected to the electrical circuit. The top row in Fig. 21 (a) presents the optical images of the wear tracks of the three rings, row (b) the wear profiles measured by contact profilometry and row (c) the 3D maps.

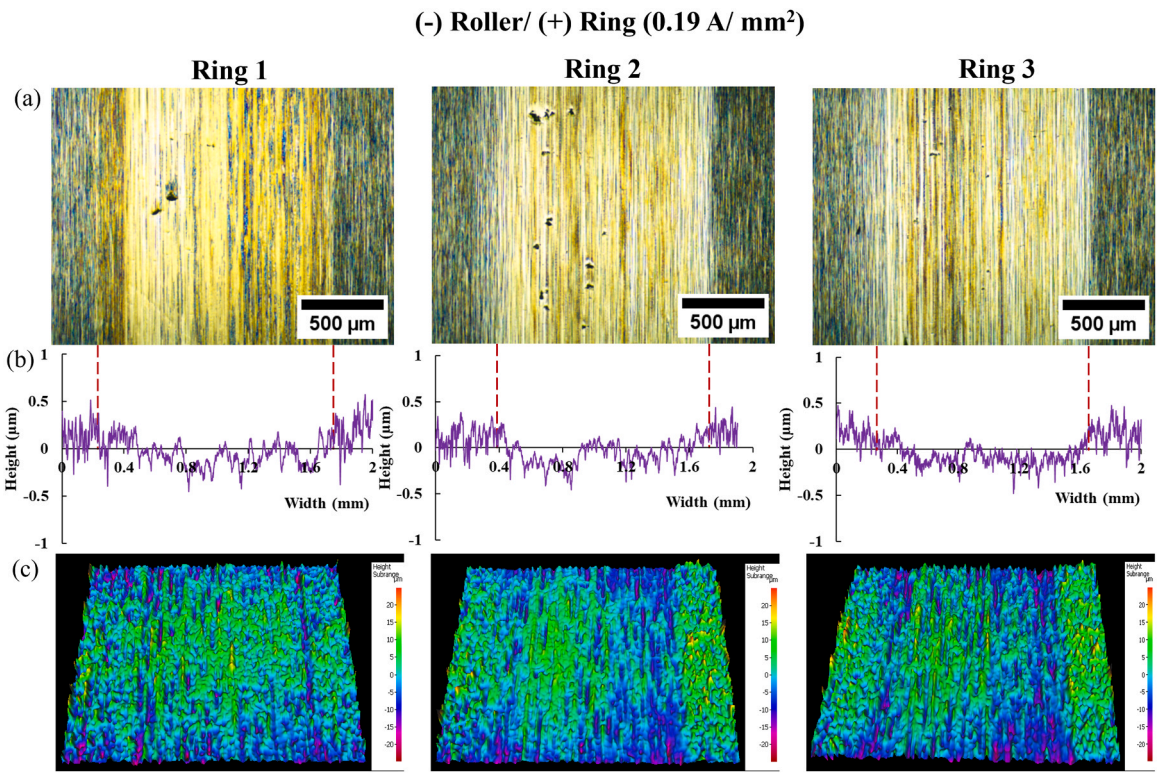

Fig. 21. Wear tracks on the three MPR rings after 322 million contact cycles in (-) Roller/ (+) Ring configuration and 0.19 A/mm^2 a) Optical images (b) Stylus wear profiles measured across the wear track, (c) Alicona 3D maps. Ring 1 is connected to the circuit.

Table 11
Wear track width of the MPR roller and rings.

Specimen	Roller	Ring 1	Ring 2	Ring 3
Width (µm) ± SD	1307.2 ± 16.5	1411.3 ± 18.7	1356.8 ± 30.7	1369.07 ± 31.8

The optical images reveal that the ring connected to the circuit exhibits a tribofim with more intensely coloured areas than rings 2 and 3 that are covered by paler and streaky tribofilms. Micro-pits are present on all three rings, with a greater density on rings 2 and 3. The profiles measured across the tracks reveal a wear depth of ~ 0.7 µm. The 3D maps show a different tribofilm distribution and thickness on the rings. The tribofilm is distributed across the entire wear track of ring 1, while it covers only half of the wear track of rings 2 and 3. The uniform tribofilm on ring 1 is the result of its positive polarity and ability to attract anions such as phosphates, carboxylates etc. intimately involved in the generation of the chemical tribofilm.

The average width of the wear track on the roller and rings measured by ImageJ software are presented in Table 11. The roller and ring wear tracks are wider than in the 'No applied electrical field' tests and can be explained by a combination of factors such as: COF, polarity and current density, which result in greater friction and Joule heating and, thus, in wear track widening.

Cross-sectional subsurface analysis of the rollers (Fig. 22**)** revealed the presence of WECs. The WECs run parallel to the surface at a depth of ~ 30 – 250 µm, are branched and give rise to specific WEAs. The SEM images (Fig. 23) revealed the steel microstructure in the WEA had changed from a tempered martensitic microstructure to a nanocrystalline microstructure.

WEC initiation and propagation are strongly dependent on specific factors such as current density, polarity, lubricant formulation, material purity, and the cyclic shear stresses and strains developed. The polarity determines specimen polarisation and the migration of the charged additives during testing resulting in the formation of different tribofilms. Thus, through its effect on the lubricant, polarity determines the wear mechanism, COF, and shear stress evolution. Current density affects the wear mechanism severity and predominance, and the kinetics of tribofilm formation. Lubricant formulation influences friction and thus the cyclic shear stresses present in the tribological contact. Material purity depends principally on the presence of non-metallic hard brittle inclusions. These act as a stress raiser and promote strain localisation which can lead to WEC initiation and propagation.

The results reveal that while WECs were not found in the absence of current, the negative polarisation of the roller (acts as cathode) and a low (0.19 A/mm^2) current density across the tribological contact can trigger WEC initiation and propagation. The propagation of WECs parallel to the surface and localised at a depth of approximately 30–250 µm can be related to the cyclic shear stresses which act parallel to the surface and reach a maximum value at a depth of 190 µm (calculated for the MPR condition employed in this study). The cathode roller leads to the absence/thin tribofilms and promotes wavelets and micro-pitting wear mechanisms. The wavelets with their peak and valley pattern increase the friction between the interacting surfaces, which affect the shear stress. The low current density of (0.17 A/mm^2) across the tribological contact leads to the formation of wavelets which are insufficient to result in early failure but increase vibrations and affect the shear stress over a larger number of contact cycles. Hence, the current density and polarity affect the COF, tribofilm formation and wear mechanism. These result in higher cyclic shear stresses and shear strains. The high cyclic shear stresses interact with non-metallic inclusions, promoting strain localisation and WEC formation.

3.3.2. Effect of high current density across the tribological contact

3.3.2.1. Characteristics of the tribofilm generated by lubricant. Tribological tests were performed in the MTM using an external voltage of

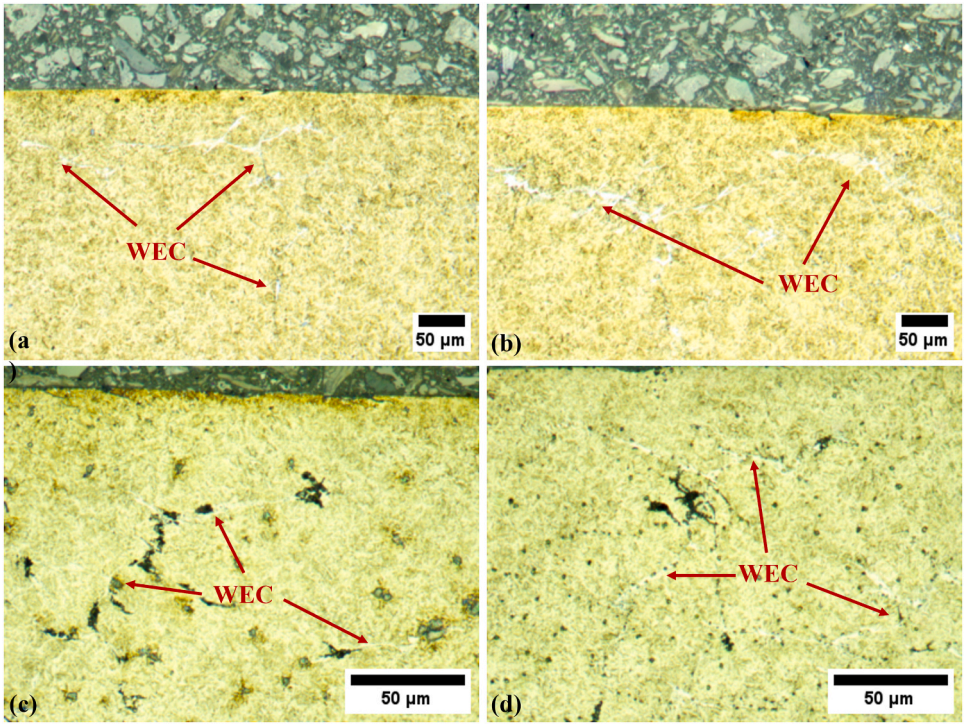

Fig. 22. Micrographs of WECs observed beneath the wear tracks in subsurface analysis of the rollers after 288 hours/ 322 contact cycles in the (-) Roller/ (+) Ring configuration with 0.19 A/mm^2.

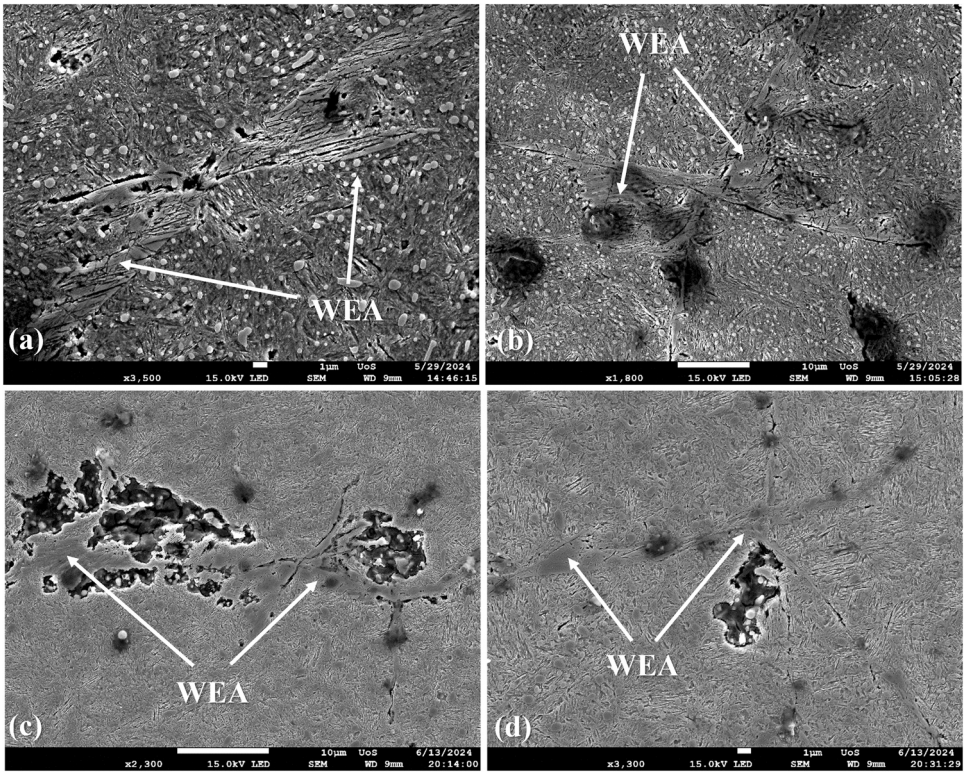

Fig. 23. SEM images of the etched specimens that reveal the microstructure of the WEAs and WECs initiating from inclusions after 288 hours/ 322 contact cycles in (-) Roller/ (+) Ring configuration with 0.19 A/mm^2.

+ 1.4 V and a 10 Ω external resistor which results in a positive voltage on the disc and negative voltage on the ball. These conditions result in a current density across the tribological contact of 1.3 A/mm^2 and lubricant breakdown.

Fig. 24 illustrates the Stribeck curves for the lubricant and the corresponding SLIM interferometry images. The SLIM images are similar to those recorded in the low current density (-) Ball/ (+) Disc case. The cathode ball does not produce a tribofilm on the wear track, but the

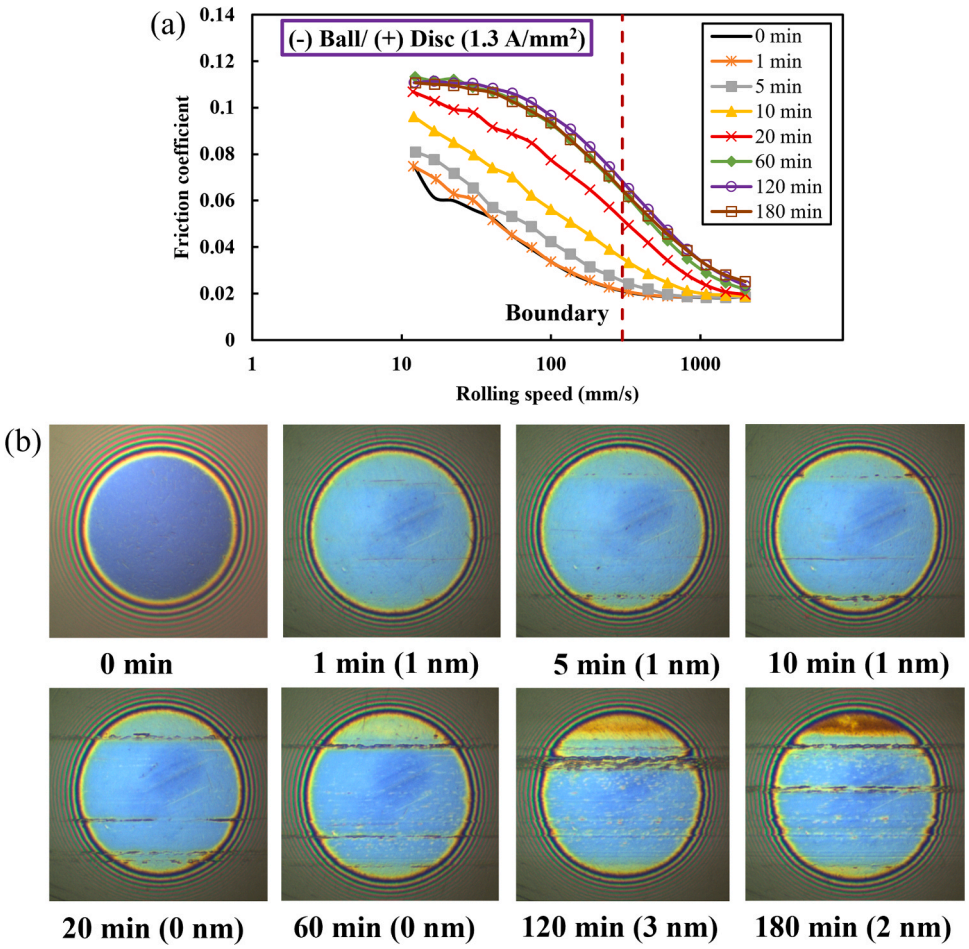

Fig. 24. MTM test results measured after 0, 1, 5, 10, 20, 60, 120, and 180 minutes of testing at 100°C with 1.3 A/mm^2 in contact (a) Stribeck curves, (b) SLIM interferometry images of the ball track.

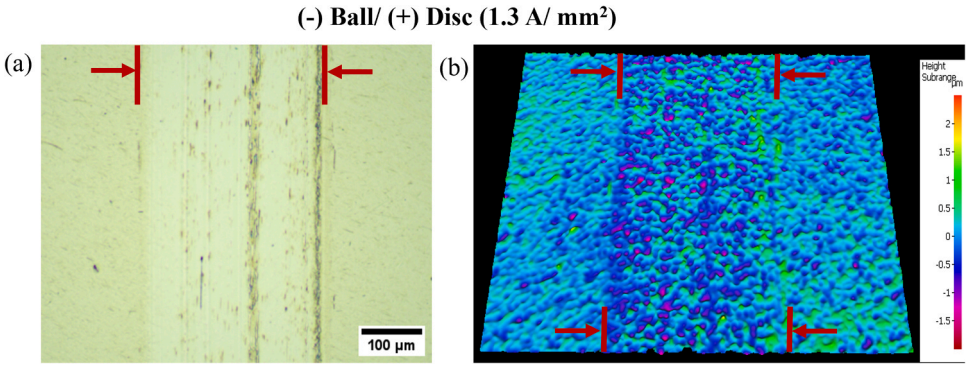

Fig. 25. Tribofilm generated on the MTM ball after 3 h conditioning time. (a) Optical image, (b) Alicona 3D map. The red arrows indicate the wear track.

film/deposit outside the track looks thicker in the high current density (1.3 A/mm^2) test than the low current density (0.17 A/mm^2). This film was not observed after the balls were cleaned (Fig. 25) which leads to the conclusion that it was not chemically bonded to the steel.

As found in the low-density current test of the same polarity, a tribofilm progressively formed on the disc which gave rise to the increase of COF shown by the Stribeck curves. The friction evolution reveals that the kinetics of tribofilm formation is higher in the first 60 minutes of testing, following which tribofilm growth is slower. The COF at 10 mm/s was 0.074 at the beginning and 0.11 at the end of the test. The COFs are approximately the same in low- and high-density current conditions, which demonstrates that the current density has only a small effect on tribofilm formation in the (-) Ball/ (+) Disc configuration.

The tribofilm streaks revealed by the SLIM interferometry images of the ball wear track were confirmed by the optical imaging and the 3D mapping (Fig. 25).

Optical and SEM images along with the profile of the disc wear track post testing are shown in Fig. 26. Compared to the test with the same polarity but lower current density, the tribofilm produced by the higher current density is thicker.

The mean values of the tribofilm thickness on the MTM disc and balls are listed in Table 12.

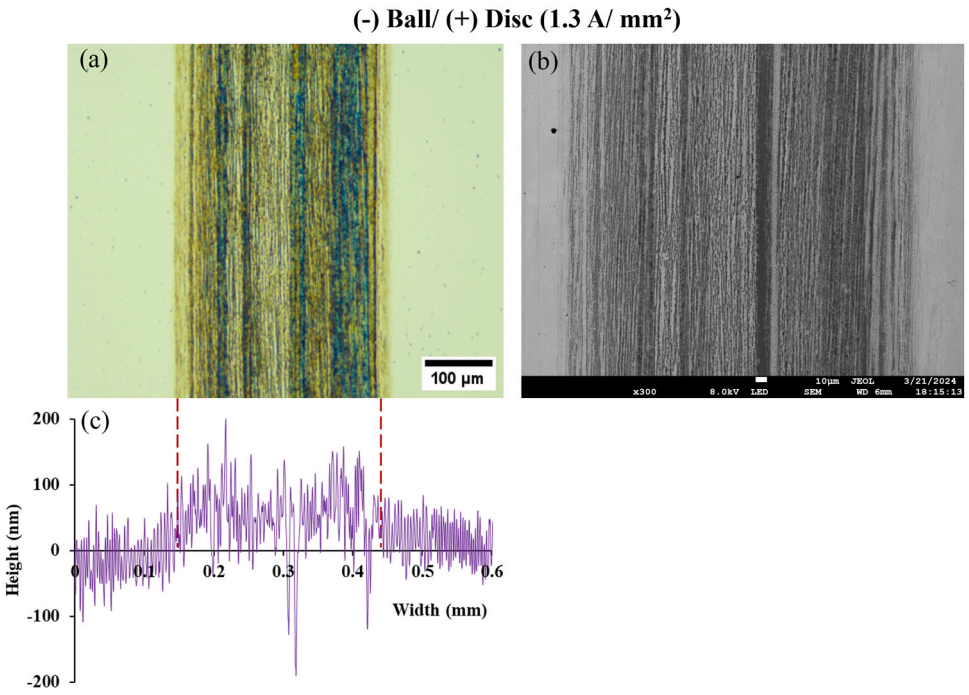

Fig. 26. Wear track on MTM disc after 3 h of rubbing (a) Optical image of the tribofilm, (b) SEM image of the tribofilm, (c) Stylus wear profiles measured across the wear track.

Table 12
Average film thickness measured on the MTM ball (SLIM) and MTM disc (contact profilometer).

	Tribofilm thickness and standard deviation (nm)
Ball (SLIM)	3 ± 1.4
Disc (Stylus profilometer)	42.4 ± 6.6

Fig. 27 presents the SEM-EDS elemental composition of the tribofilm formed on the anode (+) disc wear track. The elemental mapping shows a higher concentration of phosphorus and oxygen generated by the higher current density across the contact.

Fig. 28 presents the electrical parameters (intensity and voltage) measured across the tribological contact during the testing. The intensity curve shows a similar behaviour to the same polarity low current density test, namely a higher current intensity at the beginning of the test which then decreases in the first 60 minutes of testing followed by a region with no fluctuations. The resistance graph (Fig. 29**.a**) shows a slow and steady increase in resistance with time resulting from the growth of the tribofilm on the disc during the 'conditioning stage'. The 'Resistance Stribeck curves' (resistance versus speed) in Fig. 29**.b**. show a steady gradual increase of resistance with rolling speed/lubricant film thickness all the way into the EHD regime (1.5 m/s), and also with the rubbing time. There is an increase in resistance during the first 60 minutes of testing, whilst later the resistance stabilises, which reveals the insulating properties of the tribofilm formed. As the values of the external resistance were different in the low- and high-density current tests, the resistance values measured across the tribological contact cannot be directly compared. The trends are similar but the 'resistance Stribeck curves' measured under high current density show a more defined continuous increase with time.

The mean values for intensity, voltage and resistance were calculated from the measured/ calculated data and are presented in Table 13.

3.3.2.2. Wear mechanism and its evolution. MPR rolling contact fatigue tests with an applied voltage of – 3 V and a 5 Ω external resistor were carried out. These conditions result in a negative voltage on the roller and a positive voltage on the ring, a current density of 0.8 A/mm^2 across the tribological contact and oil film breakdown.

The test ran for 74.7 hours/ 83.7 million contact cycles until the trip conditions of Peak-to-Peak acceleration of 15 g were exceeded. Fig. 30 shows the post-test analysis of the roller specimen with optical microscopy, SEM-EDS, and profilometry.

The optical and SEM images, profile and 3D mapping reveal the

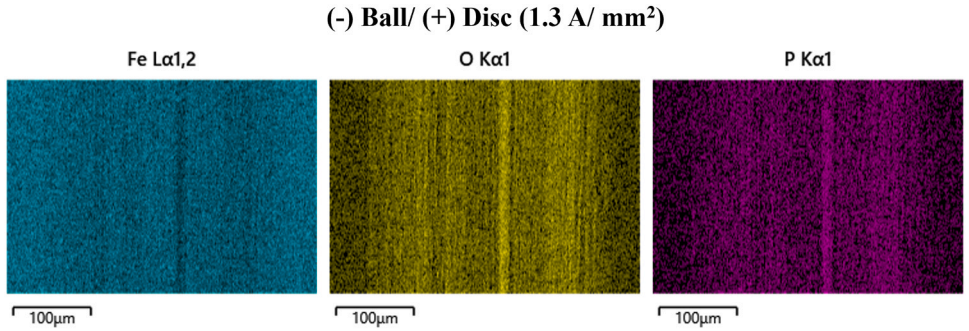

Fig. 27. EDS analysis of the wear track on the disc specimen after 3 h of rubbing in (-) Ball/ (+) Disc configuration and 1.3 A/mm^2.

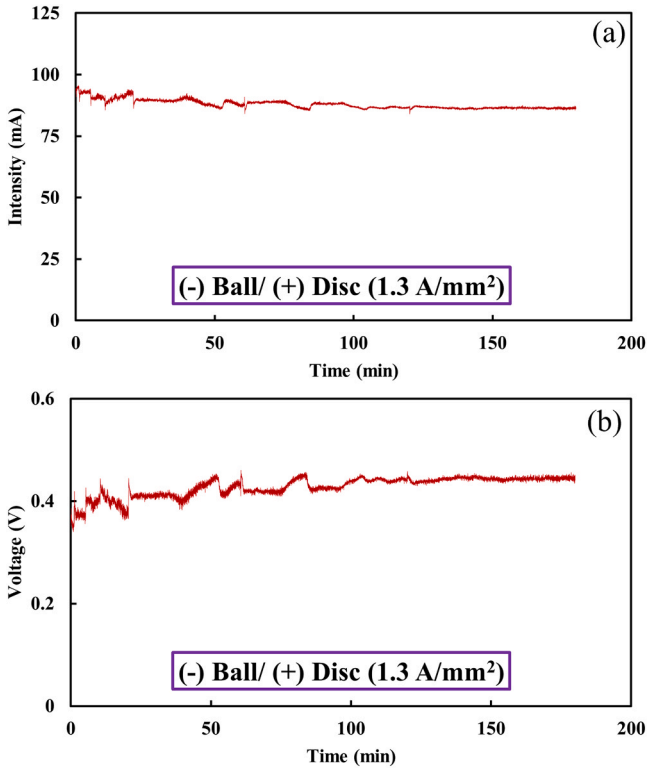

Fig. 28. Electrical parameters measured with the electrical setup during the 3 h test with (-) Ball/ (+) Disc configuration and 1.3 A/mm^2 across the tribological contact: (a) Intensity and (b) Voltage.

Table 13
Average values for intensity, voltage, and resistance in the MTM ball/disc contact.

	Mean values and standard deviation
Intensity (mA)	89.3 ± 3.5
Voltage (V)	0.4 ± 0.04
Resistance (Ω)	4.6 ± 0.6

presence of wavelet formation and micro-pits. Compared to the test with the same polarity (-) Roller (+) Ring but low current density (0.19 A/mm^2) and which ran for the entire test procedure, the current test suffered early failure from severe damage on the roller wear track. The micro-pitting areas of the track had a denser distribution of the micro-pits than that recorded at a lower current density; the amplitude of the wavelets was also greater. The increased height of the wavelets and the severe micro-pitting resulted in greater vibrations and led to early failure. Thus, higher current density results in shorter RCF life.

The measured intensity and voltage and the calculated resistance values across the MPR contact during the testing period are plotted against contact cycles in Fig. 31**.** During the first 20 minutes the intensity decreased while the voltage increased, a similar behaviour to that recorded during the MTM test. The consequential increase in contact resistance implies a gradual tribofilm formation. (Fig. 31**.c**).

The EDS elemental and mass percent composition of the wear track tribofilm are presented in Table 14. The area of wavelets had a higher concentration of C, P, O and N than the lower current density tribofilms which indicates that the tribofilm thickness increases with current density.

The optical images, profiles and 3D maps for the rings wear track are depicted in Fig. 32. Similar to the previous tests, ring 1 was connected to the electrical circuit, while rings 2 and 3 were not. The optical images

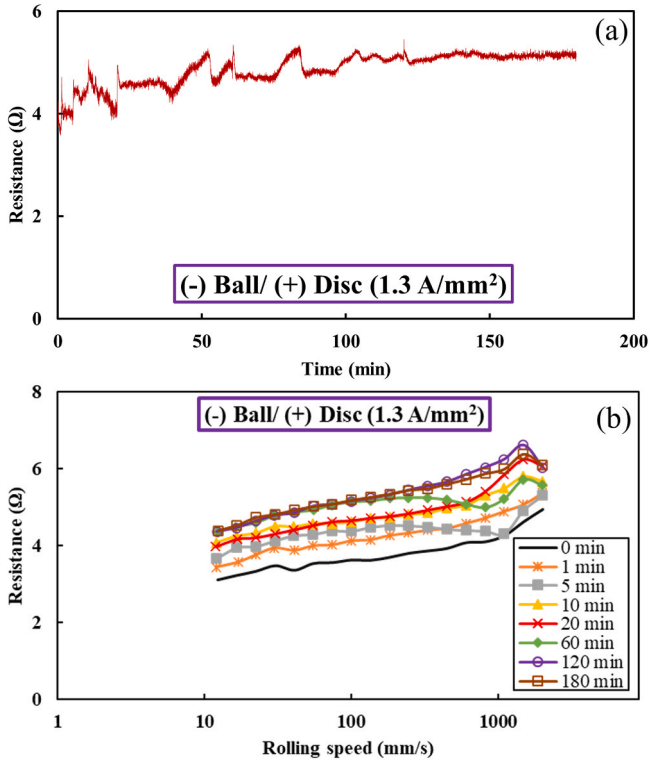

Fig. 29. Resistance measured in MTM tribological contact with (-) Ball/ (+) Disc configuration and 1.3 A/mm^2 at the tribological contact (a) Resistance across the contact (b) Resistance vs rolling speed/film thickness after 0, 1, 5, 10, 20, 60, 120, and 180 minutes of testing.

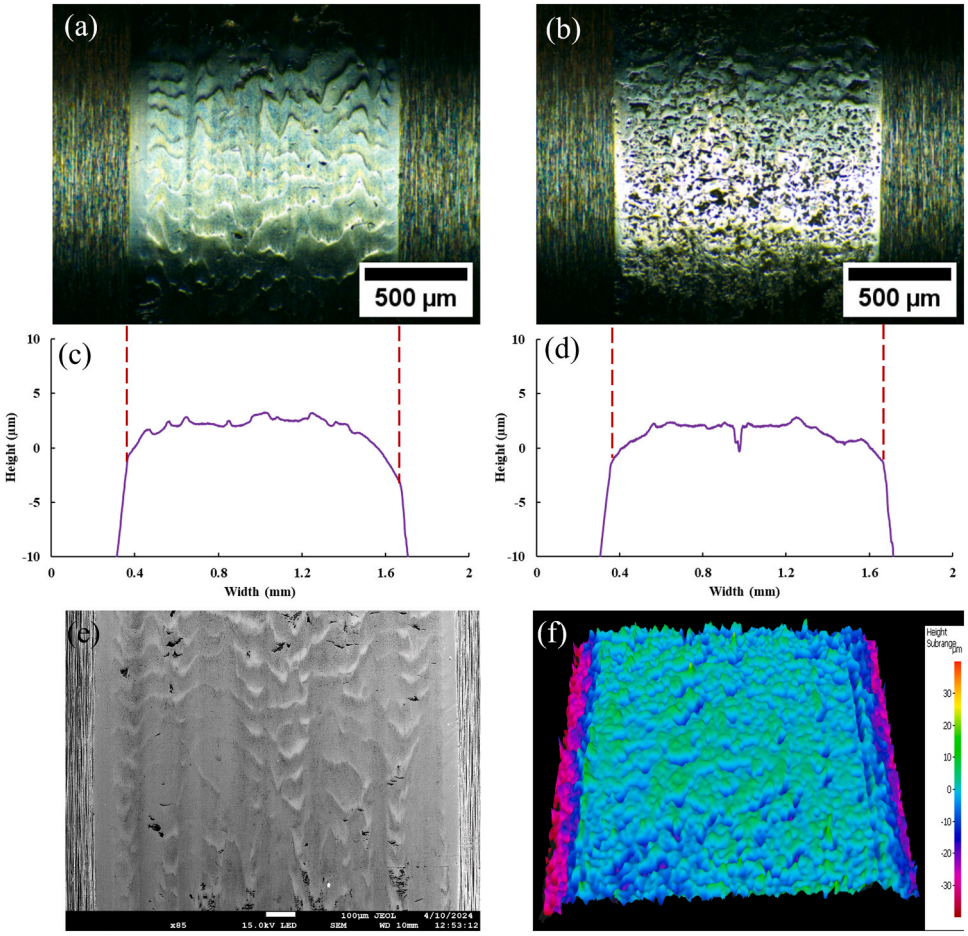

Fig. 30. MPR Roller wear track after 74.7 h/ 83.7 million contact cycles in (-) Roller/ (+) Ring configuration and 0.8 A/mm^2 current density: (a) Optical image, (b) Stylus profile across the wear track, (c) SEM image, and (d) Alicona 3D map.

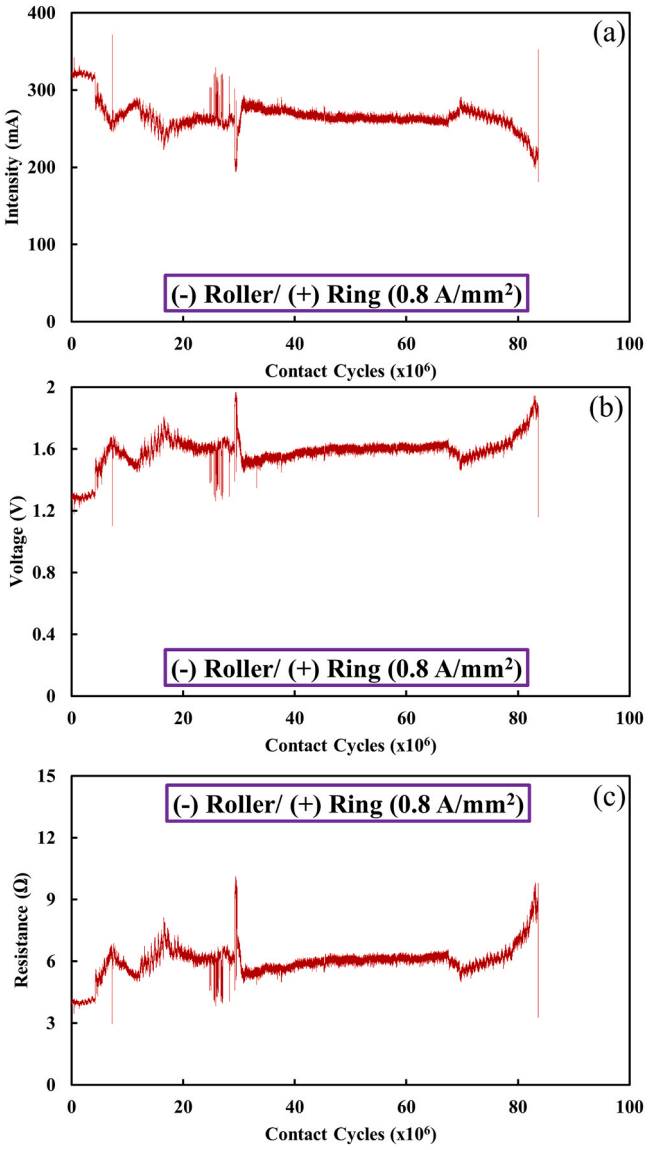

Fig. 31. Electrical parameters measured across the MPR tribological contact for (-) Roller/ (+) Ring configuration and 0.8 A/mm^2 (a) intensity, (b) voltage and (c) calculated resistance.

Table 14
SEM/EDX elemental and mass% composition of the roller tribofilm.

Element	Fe	Cr	O	Mn	C	P	N
mass %	83.79	1.47	6.4	0.05	6.56	1.33	0.05

reveal that the ring 1 wear track had a light blue, patched tribofilm, whilst rings 2 and 3 had dark blue coloured tribofilms with some yellow areas. The contact and optical (3D maps) profilometry results show that the neutral rings 2 and 3 suffered a greater amount of wear than ring 1 that functioned as an anode. The positively charged ring 1 promoted the build-up of the tribofilm which protected it from wear.

The mean widths of the roller and ring wear tracks measured by ImageJ software are presented in Table 15. The wear tracks are narrower than those obtained from the same polarity low current density (0.19 A/mm^2) tests. The COF (0.045) in the higher current density test is also greater than in the lower density test.

The narrower width of the roller and ring wear tracks can be attributed to the smaller number of rolling contact cycles (83.7 million), compared to the duration of the low current density tests (322 million contact cycles). The higher COF is due to the severe damage on the roller in the form of wavelets and micro-pitting.

After metallographic preparation of the roller wear track, optical and SEM images of the subsurface damage were taken (Fig. 33). Both optical and SEM investigations revealed the presence of fatigue cracks that initiated at the surface. No WECs were found.

3.4. Comparation between neutral/cathodic polarisation and low/high current density

Fig. 34 shows a comparison between the COF measured during the 'conditioning phases' in the MTM tests in the 'No applied electrical field' and (-) Ball/ (+) Disc configuration with low/high current density.

The COF during the 'conditioning phase' gives important information regarding the effect of electrical polarity and current density across the tribological contact. If the increase in friction can be correlated to the tribofilm buildup with time, the three curves indicate that the contact polarisation and higher current densities are beneficial and lead to the faster generation of thicker tribofilms.

The comparison between the Stribeck curves measured after three

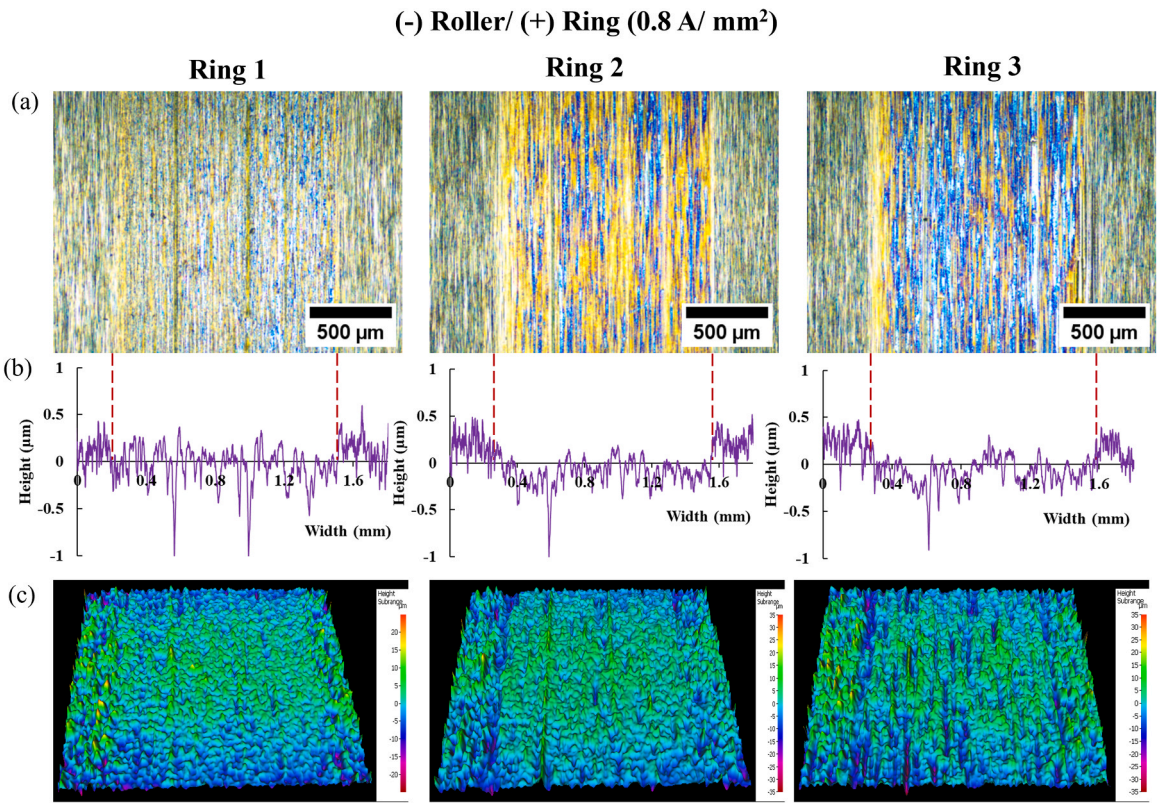

Fig. 32. Wear tracks on the three MPR rings after 336 million contact cycles in (-) Roller/ (+) Ring configuration and 0.8 A/mm^2 (a) Optical images (b) Stylus wear profiles measured across the wear track, (c) Alicona 3D maps. Ring 1 is connected to the circuit.

Table 15
Mean wear track width of the MPR roller and rings.

Specimen	Roller	Ring 1	Ring 2	Ring 3
Width (µm) ± SD	1295.3 ± 17.5	1337.5 ± 14.8	1320.5 ± 15.2	1314.1 ± 23.3

hours of rubbing in the same electrical configurations (Fig. 35) shows the same trend as the friction variation. Tests with (-) Ball/ (+) Disc configuration increased friction in the mixed and boundary regimes and generated thicker tribofilms. Current density plays an insignificant role in boundary regime.

4. Conclusions

This study investigated the effect of the electrical current on tribological contacts lubricated with a gearbox oil. The polarity and current density across the contact impacted tribofilm formation and wear mechanisms. The main findings of the study can be summarised as:

- When the applied electrical field across the tribological contact exceeds the electrical strength of the lubricant, the breakdown of the lubricant occurs, and it starts to behave as an Ohmic conductor.

  'No applied electrical field'

- In MTM tests the tribofilm growth kinetics are slow generating thin films (4 nm after 3 hours of rubbing). This outcome can be due to the anti-wear additive which does not form thick tribofilms. The RCF tests in the MPR completed the testing procedure and the associated wear mechanism was micro-pitting.

  Cathodic configuration

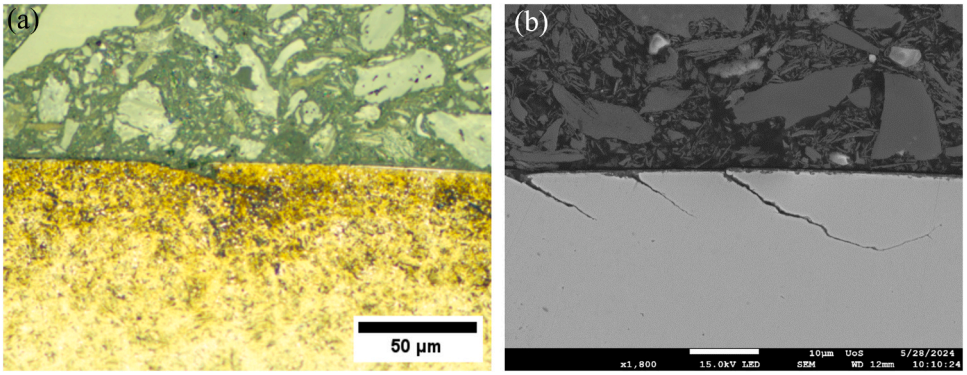

Fig. 33. Optical image of the etched microstructure (a) and SEM image (b) of the fatigue cracks in (-) Roller/ (+) Ring configuration and 0.8 A/mm^2.

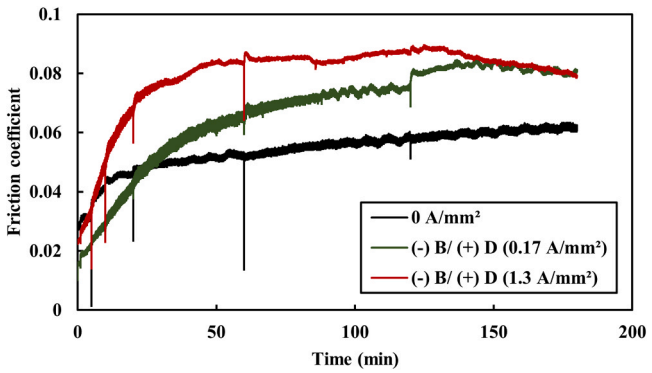

Fig. 34. Friction coefficients during the conditioning phase for 'No applied electrical field' configuration, (-) Ball/ (+) Disc configuration and 0.17 A/mm^2, (-) Ball/ (+) Disc configuration and 1.3 A/mm^2.

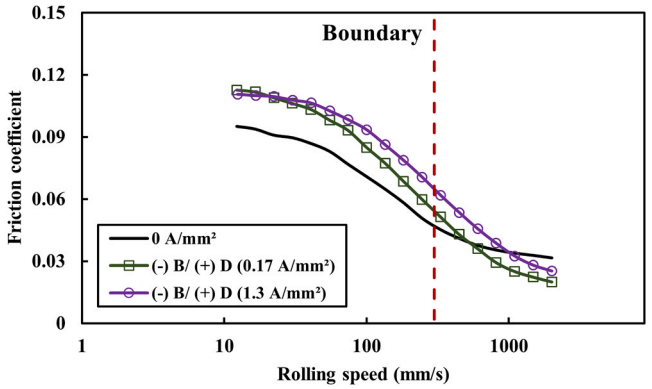

Fig. 35. Stribeck curves measured after three hours of MTM testing.

- MTM tests with (-) Ball/ (+) Disc polarity were run with low and high (0.17 and 1.3 A/mm^2) current densities to investigate tribofilm formation. This configuration leads to tribofilm growth predominantly on the disc and its thickness increases with current density. A higher COF was recorded which increased with the current density.
- MPR tests with (-) Roller/ (+) Ring polarity were carried out with low and high (0.19 and 0.8 A/mm^2) current densities to study RCF life and wear mechanisms. Under these conditions the wear mechanisms were micro-pitting and wavelets. Low current density generates sufficient cyclic shear stress from friction for WEC formation and propagation at 30–250 μm depth below the surface. WECs are surrounded by WEA, arranged parallel to the surface with cracks branching/linked to the non-metallic inclusions. At high current density, failure occurs due to severe micro-pitting and greater height wavelets.
- SEM/EDS investigation revealed that the tribofilm elemental composition depends on the polarisation. The elements predominantly found in the anode tribofilm composition are P, O, C, and S while the N was found only in the tribofilm formed on cathode The elemental concentration (mass percentage) correlates well with the tribofilm thickness.
- Under applied electrical field, the width of the MPR roller and ring wear tracks increased. This is the effect of the prolongated frictional heating and thermal expansion of the specimens which lead to increased wear.

Statement of Originality

This study investigated the effect of the electrical current on tribological contacts lubricated with a gearbox oil and showed that the polarity and current density across the contact impacted tribofilm formation and wear mechanisms. The research showed how the cathodic polarity of the ball (MTM) and roller (MPR) dramatically changes tribofilm generation, friction, wear mechanisms and RCF life as compared to 'No applied electrical field' situation. The findings contribute to designing efficient lubrication and formulating suitable lubricants for wind turbines.

We declare that the work described has not been published previously and is not under consideration for publication elsewhere. We confirm that the manuscript has been approved by all authors. We further confirm that if accepted this manuscript will not be published elsewhere in the same form without the written consent of the publisher. (134 words)

CRediT authorship contribution statement

G. Cernalevschi: Conceptualization, Data curation, Formal analysis, Investigation, Methodology, Validation, Writing – original draft, Writing – review & editing. **M. Ratoi:** Conceptualization, Data curation, Formal analysis, Funding acquisition, Investigation, Methodology, Project administration, Resources, Supervision, Validation, Writing – original draft, Writing – review & editing. **B.G. Mellor:** Conceptualization, Data curation, Formal analysis, Funding acquisition, Investigation, Methodology, Supervision, Validation, Writing – original draft, Writing – review & editing. **Y. Cai:** Data curation, Formal analysis, Project administration, Resources, Supervision, Validation, Writing – review & editing.

Funding sources

This work was supported by ExxonMobil Technology and Engineering Company.

Declaration of Competing Interest

The authors declare that they have no known competing financial interests or personal relationships that could have appeared to influence the work reported in this paper.

Data availability

Data will be made available on request.

References

[1] Energy Institute. Statistical review of world energy 2024. BP Energy Outlook 2024 2024;73:1–79.
[2] Sheng S, O'Connor R. Reliability of wind turbines. Wind Energy Engineering. Elsevier; 2023. p. 195–211. https://doi.org/10.1016/B978-0-323-99353-1.00016-5.
[3] Dao C, Kazemtabrizi B, Crabtree C. Wind turbine reliability data review and impacts on levelised cost of energy. Wind Energy Dec. 2019;22(12):1848–71. https://doi.org/10.1002/we.2404.
[4] Peng H, Zhang H, Shangguan L, Fan Y. Review of tribological failure analysis and lubrication technology research of wind power bearings. Polym (Basel) Jul. 2022; 14(15):3041. https://doi.org/10.3390/polym14153041.
[5] Liu Z, Zhang L. A review of failure modes, condition monitoring and fault diagnosis methods for large-scale wind turbine bearings. Measurement Jan. 2020;149: 107002. https://doi.org/10.1016/j.measurement.2019.107002.
[6] Perez M, Boisseau S, Geisler M, Despesse G, Reboud JL. A triboelectric wind turbine for small-scale energy harvesting. J Phys Conf Ser Nov. 2016;773:012118. https://doi.org/10.1088/1742-6596/773/1/012118.
[7] Hernández YM, Tsovilis TE, Asimakopoulou F, Politis Z, Barton W, Lozano MM. A simulation approach on rotor blade electrostatic charging and its effect on the lightning overvoltages in wind parks. Electr Power Syst Res Oct. 2016;139:22–31. https://doi.org/10.1016/j.epsr.2015.11.039.
[8] Lopez JA, Montanya J, van der Velde O, Fabro F, Romero D. Fair weather induced charges and currents on tall wind turbines and experiments with kites. 2016 33rd International Conference on Lightning Protection (ICLP). IEEE; Sep. 2016. p. 1–4. https://doi.org/10.1109/ICLP.2016.7791446.
[9] Davis MS, Madani MR. Investigation into the Effects of Static Electricity on Wind Turbine Systems. 2018 6th International Renewable and Sustainable Energy

Conference (IRSEC). IEEE; Dec. 2018. p. 1–7. https://doi.org/10.1109/IRSEC.2018.8703008.
[10] Davis MS, Madani MR. Channeling of Static Electricity Within Wind Turbines for Transmission into the Power Grid. 2018 6th International Renewable and Sustainable Energy Conference (IRSEC). IEEE; Dec. 2018. p. 1–6. https://doi.org/10.1109/IRSEC.2018.8702878.
[11] Zhao J, Xu X, Carlson O. Electrostatic discharge impacts on the main shaft bearings of wind turbines. Wind Energy Sci Dec. 2023;8(12):1809–19. https://doi.org/10.5194/wes-8-1809-2023.
[12] Fontanes P, Montanyà J, Arcanjo M, Guerra-Garcia C, Tobella G. Experimental investigation of the electrification of wind turbine blades in fair-weather and artificial charge-compensation to mitigate the effects. J Electro Jan. 2022;115:103669. https://doi.org/10.1016/j.elstat.2021.103669.
[13] de Canha D, Cronje WA, Meyer AS, Hoffe SJ. The Use of an Electromagnetic Finite Elements Package to Aid in Understanding Shaft Voltages in a Synchronous Generator. 2007 IEEE Power Engineering Society Conference and Exposition in Africa - PowerAfrica. IEEE; Jul. 2007. p. 1–6. https://doi.org/10.1109/PESAFR.2007.4498112.
[14] Plazenet T, Boileau T, Caironi C, Nahid-Mobarakeh B. A comprehensive study on shaft voltages and bearing currents in rotating machines. IEEE Trans Ind Appl Jul. 2018;54(4):3749–59. https://doi.org/10.1109/TIA.2018.2818663.
[15] He Y, Yang P-J, Sun K, Xu Z-L, Wang H-P, He X-L, Gerada D. Impact of stator interturn short circuit fault on shaft voltage in a synchronous generator. IET Electr Power Appl Mar 2023;17(3):381–91. https://doi.org/10.1049/elp2.12271.
[16] Zitzelsberger J, Hofmann W, Wiese A, Stupin P. Bearing currents in doubly-fed induction generators. 2005 European Conference on Power Electronics and Applications. IEEE; 2005. p. 9. https://doi.org/10.1109/EPE.2005.219685.
[17] Adabi J, Zare F. Analysis, calculation and reduction of shaft voltage in induction generators. Renew Energy Power Qual Apr. 2009;1(07):13–8. https://doi.org/10.24084/repqj07.207.
[18] Liu R, Ma X, Ren X, Cao J, Niu S. Comparative analysis of bearing current in wind turbine generators. Energies May 2018;11(5):1305. https://doi.org/10.3390/en11051305.
[19] Zhi Y, Li Y, Yan G, Gao Z, Qiu L, Fang Y. Review of Motor Bearing Currents in Inverter Drive System. 2022. p. 672–83. https://doi.org/10.1007/978-981-19-1532-1_71.
[20] Ma J, Xue Y, Han Q, Li X, Yu C. Motor Bearing Damage Induced by Bearing Current: A Review. Machines Dec. 2022;10(12):1167. https://doi.org/10.3390/machines10121167.
[21] Kriese M, Wittek E, Gattermann S, Tischmacher H, Poll G, Ponick B. Influence of bearing currents on the bearing lifetime for converter driven machines. 2012 XXth International Conference on Electrical Machines. IEEE; Sep. 2012. p. 1735–9. https://doi.org/10.1109/ICElMach.2012.6350115.
[22] Tischmacher H, Gattermann S, Kriese M, Wittek E. Bearing wear caused by converter-induced bearing currents. IECON 2010 - 36th Annual Conference on IEEE Industrial Electronics Society. IEEE; Nov. 2010. p. 784–91. https://doi.org/10.1109/IECON.2010.5675212.
[23] Didenko T, Pridemore WD. Electrical fluting failure of a tri-lobe roller bearing. J Fail Anal Prev Oct. 2012;12(5):575–80. https://doi.org/10.1007/s11668-012-9598-5.
[24] Liu W. The prevalent motor bearing premature failures due to the high frequency electric current passage. Eng Fail Anal Oct. 2014;45:118–27. https://doi.org/10.1016/j.engfailanal.2014.06.021.
[25] Chiou Y-C, Lee R-T, Lin C-M. Formation criterion and mechanism of electrical pitting on the lubricated surface under AC electric field. Wear Dec. 1999;236(1–2):62–72. https://doi.org/10.1016/S0043-1648(99)00264-1.
[26] He F, Xie G, Luo J. Electrical bearing failures in electric vehicles. Friction Feb. 2020;8(1):4–28. https://doi.org/10.1007/s40544-019-0356-5.
[27] Zhang T, Du J, Lei Y, Yi X, Yin J, Yu P. Contributing to the understanding of the dielectric breakdown channel of alumina under high voltage. Ceram Int Sep. 2019;45(13):16608–11. https://doi.org/10.1016/j.ceramint.2019.05.200.
[28] Malec D, Bley V, Talbi F, Lalam F. Contribution to the understanding of the relationship between mechanical and dielectric strengths of Alumina. J Eur Ceram Soc Nov. 2010;30(15):3117–23. https://doi.org/10.1016/j.jeurceramsoc.2010.07.024.
[29] López-Uruñuela FJ, Fernández-Díaz B, Pagano F, López-Ortega A, Pinedo B, Bayón R, Aguirrebeitia J. Broad review of 'White Etching Crack' failure in wind turbine gearbox bearings: Main factors and experimental investigations. Int J Fatigue Apr. 2021;145:106091. https://doi.org/10.1016/j.ijfatigue.2020.106091.
[30] Evans M-H. White structure flaking (WSF) in wind turbine gearbox bearings: Effects of 'butterflies' and white etching cracks (WECs). Mater Sci Technol Jan. 2012;28(1):3–22. https://doi.org/10.1179/026708311X13135950699254.
[31] Richardson AD, Evans M-H, Wang L, Wood RJK, Ingram M, Meuth B. The evolution of white etching cracks (WECs) in rolling contact fatigue-tested 100Cr6 Steel. Tribol Lett Mar. 2018;66(1):6. https://doi.org/10.1007/s11249-017-0946-1.
[32] Demas NG, Lorenzo-Martin C, Luna R, Erck RA, Greco AC. The effect of current and lambda on white-etch-crack failures. Tribol Int Nov. 2023;189:108951. https://doi.org/10.1016/j.triboint.2023.108951.
[33] Steinweg F, Mikitisin A, Oezel M, Schwedt A, Janitzky T, Hallstedt B, Broeckmann C, Mayer J. Formation of white etching cracks under electrical current flow - influence of load, slip and polarity. Wear 2022:504–5. https://doi.org/10.1016/j.wear.2022.204394. 204394.
[34] Loos J, Bergmann I, Goss M. Influence of high electrical currents on wec formation in rolling bearings. Tribol Trans Jul. 2021;64(4):708–20. https://doi.org/10.1080/10402004.2021.1909789.
[35] Gould B, Demas N, Erck R, Lorenzo-Martin MC, Ajayi O, Greco A. The effect of electrical current on premature failures and microstructural degradation in bearing steel. Int J Fatigue Apr. 2021;145:106078. https://doi.org/10.1016/j.ijfatigue.2020.106078.
[36] Loos J, Bergmann I, Goss M. Influence of currents from electrostatic charges on wec formation in rolling bearings. Tribol Trans Sep. 2016;59(5):865–75. https://doi.org/10.1080/10402004.2015.1118582.
[37] Mikami H, Kawamura T. Influence of Electrical Current on Bearing Flaking Life. Apr. 2007. https://doi.org/10.4271/2007-01-0113.
[38] Sanchez LJ, Hager CH, Evans RD. Rolling element bearing damage in the presence of applied electric current. Tribol Trans May 2024;67(3):602–13. https://doi.org/10.1080/10402004.2024.2364724.
[39] Hosenfeldt B, Tim, Bugiel Christoph, Leimann Dirk-Olaf, Loos Jörg, Luther Rolf, Merk Daniel, Seyfert Christian, Shakhvorostov Dmitry, Stadler Kenred, Vengudusamy Balasubramaniam, Wiersch Petra, Wincierz Christoph, Woestmann Anne, Br. WhitE Etching Cracks - Position Paper of the German Society for Tribology. Ges FüR Tribol e V 2024. https://doi.org/10.13140/RG.2.2.27783.41121.
[40] Romanenko A, Muetze A, Ahola J. Effects of electrostatic discharges on bearing grease dielectric strength and composition. IEEE Trans Ind Appl Nov. 2016;52(6):4835–42. https://doi.org/10.1109/TIA.2016.2596239.
[41] Romanenko A, Ahola J, Muetze A. Influence of electric discharge activity on bearing lubricating grease degradation. 2015 IEEE Energy Conversion Congress and Exposition (ECCE). IEEE; Sep. 2015. p. 4851–2. https://doi.org/10.1109/ECCE.2015.7310344.
[42] Danielsen HK, Gutiérrez Guzmán F, Dahl KV, Li YJ, Wu J, Jacobs G, Burghardt G, Fæster S, Alimadadi H, Goto S, Raabe D, Petrov R. Multiscale characterization of White Etching Cracks (WEC) in a 100Cr6 bearing from a thrust bearing test rig. Wear Jan 2017;370:73–82. https://doi.org/10.1016/j.wear.2016.11.016.
[43] Ruellan A, Kleber X, Ville F, Cavoret J, Liatard B. Understanding white etching cracks in rolling element bearings: Formation mechanisms and influent tribochemical drivers. Proc Inst Mech Eng Part J J Eng Tribol Aug. 2015;229(8):886–901. https://doi.org/10.1177/1350650114557710.
[44] Gould B, Greco A. The influence of sliding and contact severity on the generation of white etching cracks. Tribol Lett Nov. 2015;60(2):29. https://doi.org/10.1007/s11249-015-0602-6.
[45] Haque T, Korres S, Carey JT, Jacobs PW, Loos J, Franke J. Lubricant effects on white etching cracking failures in thrust bearing rig tests. Tribol Trans Nov. 2018;61(6):979–90. https://doi.org/10.1080/10402004.2018.1453571.
[46] Clarke A, Evans H, Snidle R. Understanding micropitting in gears. Proc Inst Mech Eng Part C J Mech Eng Sci Apr. 2016;230(7–8):1276–89. https://doi.org/10.1177/0954406215606934.
[47] Hasan M, Mohammed OD, Kolar C, Björling M, Larsson R. Study of wear and micropitting in rolling/sliding contacts operating under boundary lubrication conditions. Procedia Struct Integr 2022;42:1169–76. https://doi.org/10.1016/j.prostr.2022.12.149.